J. Fluid Mech. (1997), *vol.* 353, *pp.* 221–259. Printed in the United Kingdom

Influence of camber on sound generation by airfoils interacting with high-frequency gusts

By MATTHEW R. MYERS[1] AND E. J. KERSCHEN[2]

[1]Hydrodynamics and Acoustics Branch, Center for Devices and Radiological Health, US Food and Drug Administration, HFZ-132, Rockville, MD 20817, USA

[2]Department of Aerospace and Mechanical Engineering, University of Arizona, Tucson, AZ 85721, USA

(Received 14 April 1996 and in revised form 4 August 1997)

A theoretical model is developed for the sound generated when a convected disturbance encounters a cambered airfoil at non-zero angle of attack. The model is a generalization of a previous theory for a flat-plate airfoil, and is based on a linearization of the Euler equations about the steady, subsonic flow past the airfoil. High-frequency gusts, whose wavelengths are short compared to the airfoil chord, are considered. The airfoil camber and incidence angle are restricted so that the mean flow past the airfoil is a small perturbation to a uniform flow. The singular perturbation analysis retains the asymptotic regions present in the case of a flat-plate airfoil: local regions, which scale on the gust wavelength, at the airfoil leading and trailing edges; a 'transition' region behind the airfoil which is similar to the transition zone between illuminated and shadow regions in optical problems; and an outer region, far away from the airfoil edges and wake, in which the solution has a geometric-acoustics form. For the cambered airfoil, an additional asymptotic region in the form of an acoustic boundary layer adjacent to the airfoil surface is required in order to account for surface curvature effects. Parametric calculations are presented which illustrate that, like incidence angle, moderate amounts of airfoil camber can significantly affect the sound field produced by airfoil–gust interactions. Most importantly, the amount of radiated sound power is found to correlate very well with a single aerodynamic loading parameter, α_{eff}, which is an effective mean-flow incidence angle for the airfoil leading edge.

1. Introduction

Sound generated through the unsteady interaction of convected disturbances (gusts) with airfoils is a problem of importance in a number of aeroacoustic applications. Most analyses of airfoil–gust interactions have utilized the classical linearized approach, in which the total flow is represented as the sum of a uniform flow, an $O(\alpha)$ (relative to the uniform field) steady disturbance, and an $O(\epsilon)$ unsteady disurbance. If α and ϵ are small and of the same order, the $O(\alpha)$ perturbation to the mean flow can be ignored in analysing the unsteady flow. However, in many cases the steady aerodynamic loading of the airfoils is quite large so that $\alpha \gg \epsilon$, and it then becomes desirable to account for the effects of the mean-flow distortion on the unsteady motion.

In a previous paper (Myers & Kerschen 1995, hereafter referred to as MK95)

we examined the influence of one contribution to the steady aerodynamic loading, the airfoil incidence angle, on the sound generated by the interaction of airfoils with convected disturbances. We concentrated on the case of a mean flow which is compressible but subsonic, and a gust wavelength which is short compared to the airfoil chord. This paper extends the theory of MK95 to include the other contribution to the airfoil steady loading, the airfoil camber. Typically, the incidence angle, camber, and thickness of an airfoil are of the same order of magnitude, and introduce effects of comparable importance on the sound field. However, it will be seen in this paper that the effects of incidence angle and camber, which determine the steady loading, combine in a natural way. Noise source terms associated with airfoil thickness can be superposed with those due to steady loading, and will be presented in a subsequent paper. Additional discussion of previous research related to the influence of airfoil steady loading on gust–airfoil interaction noise can be found in MK95.

The approach used in MK95 is based upon Goldstein's (1978) extension of rapid-distortion theory to compressible flows. Rapid-distortion theory considers inviscid linear unsteady disturbances to an irrotational base flow. In contrast to methods based upon the acoustic analogy, there is no modelling of source terms, which becomes difficult in the high-frequency (highly non-compact) limit.

Goldstein's equations, while linear, contain variable coefficients which do not have a closed-form representation in the general case. Kerschen & Myers (1987) simplified the governing equations under the assumption of a mean flow which is a small perturbation to a uniform flow. The $O(\alpha)$ steady-flow perturbation is assumed large compared to the $O(\epsilon)$ unsteady disturbances, i.e. $\epsilon \ll \alpha \ll 1$.

In MK95, the simplified governing equations were solved for the specific case of a flat-plate airfoil at a small angle of attack. The assumptions of a high-frequency gust and a small-perturbation mean flow allowed a closed-form asymptotic solution. The singular-perturbation analysis contained four asymptotic regions: two local regions, which scale on the disturbance wavelength and reside at the leading and trailing edges of the airfoil; a 'transition region', similar to the zone between illuminated and shadow regions in optical problems, lying downstream of the airfoil at shallow angles; and an outer region away from the airfoil edges and wake, where the solution has a geometric-acoustics form.

Numerical results in MK95 showed that moderate levels of steady loading due to incidence angle can have a significant influence on the sound field. The effect is most pronounced at higher frequencies and higher Mach numbers. Analysis of the flat-plate solution also confirmed sound-generation mechanisms first analysed via the acoustic analogy (Ffowcs Williams & Hawkings 1969*a*, *b* and Ffowcs Williams & Hall 1970), specifically volume sources arising from Reynolds stress fluctuations due to interaction of the gust with mean-flow gradients, and the scattering of these quadrupole fields by the airfoil surface. In addition to confirming these mechanisms by which sound is generated through vorticity distortion, the flat-plate solution also revealed that local scattering by spatial gradients in the propagation medium can be an important sound-generating mechanism at high Mach numbers.

In this paper, the equations derived by Kerschen & Myers (1987) are solved in the high-frequency ($k \gg 1$) limit for the case of a zero-thickness cambered airfoil. The camber distribution and incidence angle of the airfoil are both $O(\alpha)$. As for the flat plate, the solution is developed as an asymptotic series based upon the small-loading and high-frequency parameters. The asymptotic regions present for a flat-plate airfoil also exist when airfoil camber is present. Treatment of airfoil curvature effects requires the introduction of an additional region, as follows.

Acoustic propagation around curved surfaces exhibits such phenomena as 'creeping waves' on convex surfaces and 'whispering galleries' on concave surfaces. These phenomena are difficult to describe in a simple mathematical form. Some of the theories are outlined in Myers & Kerschen (1992), for the related problem of a three-dimensional source in a linearly stratified medium. In the present case where the airfoil chord is small compared to its radius of curvature, a relatively simple boundary-layer theory can be employed to describe the near-surface propagation. The boundary layer is effectively an additional 'transition region', this time residing next to the airfoil surface. Like the downstream transition region, it contains features of both ray and diffraction fields.

In addition to the analysis in the new asymptotic region, some modifications to the flat-plate theory are required in the other asymptotic regions. An extensive parametric study is performed to identify the dominant factors influencing the sound field in airfoil–gust interactions. It will be shown that, under a wide range of conditions, the total sound power is well correlated by a single aerodynamic loading parameter – the effective leading-edge incidence angle, α_{eff}.

2. Formulation

2.1. *Summary of the general theory*

The equations describing the interaction of airfoils with small-amplitude convected disturbances are presented in a general form in MK95. Here we extract the most important results, and introduce slight notational changes. Details of the derivations may be found in MK95 and Kerschen & Myers (1987).

We consider convected vortical and entropic disturbances having a harmonic representation in the uniform flow of speed U_∞ far upstream,

$$\begin{bmatrix} \boldsymbol{v}' \\ s' \end{bmatrix} = \begin{bmatrix} \epsilon U_\infty (A_t, A_n, A_3) \\ 2\epsilon c_p B \end{bmatrix} \mathrm{e}^{\mathrm{i}k(\phi + k_n \psi + k_3 x_3 - t)}, \tag{2.1a}$$

where

$$k = \omega b / U_\infty \tag{2.1b}$$

is the reduced frequency of unsteady aerodynamic theory, based upon the airfoil semi-chord b. The dimensionless parameter ϵ is assumed to be small. Time is normalized by b/U_∞, and c_p is the specific heat at constant pressure. The independent variables, which are the potential-streamfunction coordinates introduced in MK95, are non-dimensionalized by

$$\phi = \phi_p / U_\infty b, \quad \psi = \beta_\infty \psi_p / U_\infty b, \quad \text{and} \quad x_3 = x_{3p}/b,$$

where ϕ_p and ψ_p are the physical potential and streamfunction and x_{3p} the spanwise position. Since the incident disturbances convect along the mean-flow streamlines, the analysis is simpified by the use of (ϕ, ψ) coordinates. The upper and lower surfaces of the airfoil are given by $\psi = 0\pm$, and $\phi = 0$ at the leading-edge stagnation point.

The disturbances are convected by a mean flow which is an $O(\alpha)$ perturbation to a uniform flow ($\epsilon \ll \alpha \ll 1$). The unsteady irrotational field, generated by the interaction of the convected disturbance with the airfoil and the non-uniform mean flow, can be described in terms of a modified potential $h(\phi, \psi)$ defined by

$$h(\phi, \psi) = \frac{G'}{\epsilon U_\infty b} \mathrm{e}^{-\mathrm{i}k(k_3 x_3 - t)} \mathrm{e}^{\mathrm{i}k M_\infty^2 \phi / \beta_\infty^2} \mathrm{e}^{-M_\infty^2 q}, \tag{2.2}$$

where G' is the physical velocity potential and $q(\phi,\psi)$ is defined in (2.4). The modified potential satisfies

$$L_0(h) + L_1(h) = kS(\phi,\psi)\mathrm{e}^{\mathrm{i}k\Omega}, \tag{2.3a}$$

where L_0 is the standard Helmholtz operator

$$L_0(h) = \frac{\partial^2 h}{\partial\phi^2} + \frac{\partial^2 h}{\partial\psi^2} + k^2 w^2 h, \tag{2.3b}$$

$$w^2 = (\delta M_\infty)^2 - (k_3/\beta_\infty)^2, \tag{2.3c}$$

M_∞ is the upstream Mach number, $\beta_\infty = (1 - M_\infty^2)^{1/2}$, and $\delta = 1/\beta_\infty^2$. The operator L_1 contains variable coefficients, and accounts for effects of the mean-flow gradients on the acoustic propagation. This operator takes the form

$$L_1(h) = \frac{(\gamma+1)M_\infty^4}{\beta_\infty^2}\left\{q\left[\frac{\partial^2 h}{\partial\psi^2} + 2\mathrm{i}k\delta\frac{\partial h}{\partial\phi} + k^2(w^2+\delta^2)h\right] - \frac{\partial q}{\partial\phi}\left[\frac{\partial h}{\partial\phi} - \mathrm{i}k\delta h\right]\right\} - 2k^2 w^2\beta_\infty^2 q h. \tag{2.3d}$$

The function $q(\phi,\psi)$ characterizing the non-uniform medium is the normalized perturbation ($O(\alpha)$) flow speed:

$$\frac{U_0}{U_\infty} = 1 + q(\phi,\psi) + O(\alpha^2), \tag{2.4}$$

where U_0 is the total mean-flow speed. The amplitude $S(\phi,\psi)$ of the source term in (2.3a) is given by

$$S(\phi,\psi) = \frac{2}{\beta_\infty^2}\left\{\mathrm{i}(A_t^* - k_n A_n\beta_\infty^3)q + \mathrm{i}(k_n A_t^*\beta_\infty^2 + A_n\beta_\infty)\mu + \frac{1}{k}\left[A_t^* M_\infty^2\frac{\partial q}{\partial\phi} + A_n M_\infty^2\beta_\infty\frac{\partial q}{\partial\psi}\right]\right\}, \tag{2.5a}$$

where $A_t^* = A_t - B$, and $\beta_\infty\mu$ is the perturbation in flow angle in the physical plane. The phase of the source term is

$$\Omega = \delta\phi + k_n\psi + g(\phi,\psi), \tag{2.5b}$$

where

$$g(\phi,\psi) = \int_{-\infty}^{\phi}\left[\frac{U_\infty^2}{U_0^2(\eta,\psi)} - 1\right]\mathrm{d}\eta. \tag{2.5c}$$

The integral $g(\phi,\psi)$ (Lighthill's Drift function) can be approximated by

$$g(\phi,\psi) = -2\mathrm{Re}\ [F(\phi + \mathrm{i}\psi)] + O(\alpha^2), \tag{2.5d}$$

where F is the perturbation complex potential for the compressible mean flow, with the arbitrary constant in F chosen such that $g \to 0$ as $\phi \to -\infty$. Since the perturbation speed q and flow angle $\beta_\infty\mu$ are $O(\alpha)$, as is the complex potential F, then the perturbation operator L_1, source amplitude $S(\phi,\psi)$, and drift function $g(\phi,\psi)$ are also $O(\alpha)$. For convenience in subsequent definitions we have not explicitly extracted the parameter α.

The boundary condition applied on the airfoil surface is

$$\left[\frac{\partial h}{\partial\psi} + M_\infty^2\frac{\partial q}{\partial\psi}h\right]_{0\leqslant\phi\leqslant\phi_{TE\pm},\psi=0\pm} = -\left[\frac{A_n}{\beta_\infty}(1 - M_\infty^2 q) - 2A_t^*\mu\right]\mathrm{e}^{\mathrm{i}k\Omega}, \tag{2.6}$$

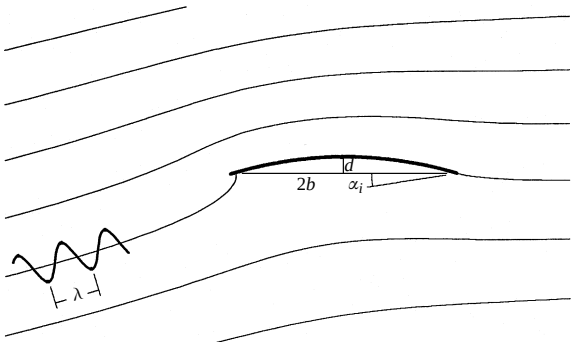

FIGURE 1. Cambered airfoil at angle of attack α_i encountering a convected disturbance. Disturbance wavelength λ is assumed to be much smaller than the airfoil chord $2b$.

where $\phi_{TE\pm}$ are the locations of the trailing edge in (ϕ, ψ)-space for the upper and lower surfaces of the airfoil, respectively. The radiation condition applies far away from the airfoil.

The modified pressure p is related to the physical unsteady pressure component p' by

$$p = \frac{-p' \mathrm{e}^{\mathrm{i}k(-k_3 x_3 + t)}}{\epsilon \rho_\infty U_\infty^2}. \tag{2.7a}$$

It is computed from the modified potential h by the relation

$$p = \left[\frac{\partial h}{\partial \phi} - \mathrm{i}k\delta h\right] \mathrm{e}^{-\mathrm{i}k\delta M_\infty^2 \phi}. \tag{2.7b}$$

2.2. *Analysis for a cambered airfoil*

The results of §2.1 apply to a general small-perturbation mean flow; we now specifically consider the problem depicted in figure 1. A cambered airfoil at incidence angle α_i encounters a convected disturbance whose wavelength is short compared to the airfoil chord. The airfoil maximum camber $d/2b$ (more relevant measures of camber will be introduced shortly) and the incidence angle α_i are assumed to be $O(\alpha)$. The reduced frequency k is assumed large; the theory is valid for $k = O(\alpha^{-\gamma})$, with $2/3 < \gamma < 2$. Note that we have changed the incidence angle from α (used in MK95) to α_i.

The functions q, μ, and g required in (2.3) are all derivable from the complex potential F for the mean-flow perturbation. The function F for a compressible flow can be obtained from the corresponding incompressible potential through a Prandtl–Glauert transformation. While the incompressible potential for a flat plate can be found through a conformal mapping, no such mapping exists for a general cambered airfoil. However, since the mean-flow quantities are only required to $O(\alpha)$ accuracy, approximate results from thin-airfoil theory can be used. The boundary condition can then be transferred from the airfoil surface to a line parallel to the upstream flow. We utilize the result of Cheng & Rott (1954), who showed that the incompressible (denoted by the superscript *in*) complex velocity is given by

$$q^{in} - \mathrm{i}\mu^{in} = -\frac{\mathrm{i}}{\pi}\left(\frac{z^{in} - 2b}{z^{in}}\right)^{1/2} \int_0^{2b} \left(\frac{s}{2b - s}\right)^{1/2} \frac{N'(s)}{z^{in} - s} \mathrm{d}s + O(\alpha^2), \tag{2.8}$$

where $z^{in} = x_1 + \mathrm{i}x_2$, the coordinates (x_1, x_2) are dimensional, and the airfoil shape

is given by $x_2 = N(x_1)$. The prime denotes differentiation. For $\alpha \ll 1$ the effects of camber and incidence can be superposed, i.e. we can set $N(x_1) = -\alpha_i x_1 + n^*(x_1)$, where $n^*(x_1)$ is the dimensional camber distribution of the airfoil, measured from the line segment connecting the leading and trailing edges. After applying a Prandtl–Glauert transformation and switching to non-dimensional potential-streamfunction coordinates, we find that (2.8) becomes

$$q - \mathrm{i}\mu = \frac{\mathrm{i}\alpha_i}{\beta_\infty}\left[1 - \left(\frac{\zeta - 2}{\zeta}\right)^{1/2}\right] - \frac{\mathrm{i}}{\pi\beta_\infty}\left(\frac{\zeta - 2}{\zeta}\right)^{1/2}\int_0^2 \left(\frac{s}{2-s}\right)^{1/2}\frac{n'(s)}{\zeta - s}\mathrm{d}s + O(\alpha^2), \tag{2.9}$$

where $\zeta = \phi + \mathrm{i}\psi$ and the non-dimensional form of the airfoil camber distribution function $n(s) = n^*/b$ is $O(\alpha)$.

The corresponding complex potential is

$$F(\zeta) = F_c(\zeta) + F_i(\zeta), \tag{2.10}$$

where F_c is the potential for a cambered airfoil at zero incidence and F_i applies to a flat-plate airfoil at incidence angle α_i (equation (3.1) of MK95):

$$F_i(\zeta) = \frac{\mathrm{i}\alpha_i}{\beta_\infty}(\log[\zeta - 1 + (\zeta(\zeta - 2))^{1/2}] + \zeta - (\zeta(\zeta - 2))^{1/2} + C_i). \tag{2.11}$$

The function F_c may be obtained by integrating the camber portion of (2.9) with respect to ζ, interchanging the order of integration, and performing the inner integration. The result is

$$F_c(\zeta) = \frac{-\mathrm{i}}{\beta_\infty \pi}\int_0^2 n'(s)\left(\frac{s}{2-s}\right)^{1/2}\left[\log\left[\frac{1 + ((\zeta - 2)/\zeta)^{1/2}}{1 - ((\zeta - 2)/\zeta)^{1/2}}\right]\right.$$
$$\left. -\mathrm{i}\left(\frac{2-s}{s}\right)^{1/2}\log\left[\frac{\mathrm{i}((2-s)/s)^{1/2} + ((\zeta - 2)/\zeta)^{1/2}}{\mathrm{i}((2-s)/s)^{1/2} - ((\zeta - 2)/\zeta)^{1/2}}\right] + C_c\right]\mathrm{d}s. \tag{2.12}$$

The arbitrary constants C_c and C_i will be specified during the various applications.

As for the flat plate, our approach to solving (2.3) is through an asymptotic series for large k and small α. We retain terms which are $O(\alpha k^{1/2}, 1/k^{1/2})$ relative to the uniform-flow result, but ignore $O(\alpha, \alpha^2 k, 1/k)$ effects. The asymptotic regions utilized in the singular-perturbation analysis are shown in figure 2(*a*). Figure 2(*b*) illustrates the potential-streamfunction coordinate systems employed in the various asymptotic regions. Relative to the corresponding figures for the flat plate, an additional boundary layer is present, lying next to the airfoil surface and beginning near the leading edge. This new region, labelled the 'leading-edge transition region', accounts for acoustic propagation near the curved surface. The boundary layer downstream of the trailing edge, present also for a flat plate, has been relabelled the 'trailing-edge transition region'. The following sections provide the details of the analysis in each of the asymptotic regions.

3. Local leading-edge region

The local leading-edge expansion of the mean-flow perturbation velocity can be readily obtained from (2.9). By inserting the local coordinates

$$\Phi = k\phi, \quad \Psi = k\psi \tag{3.1}$$

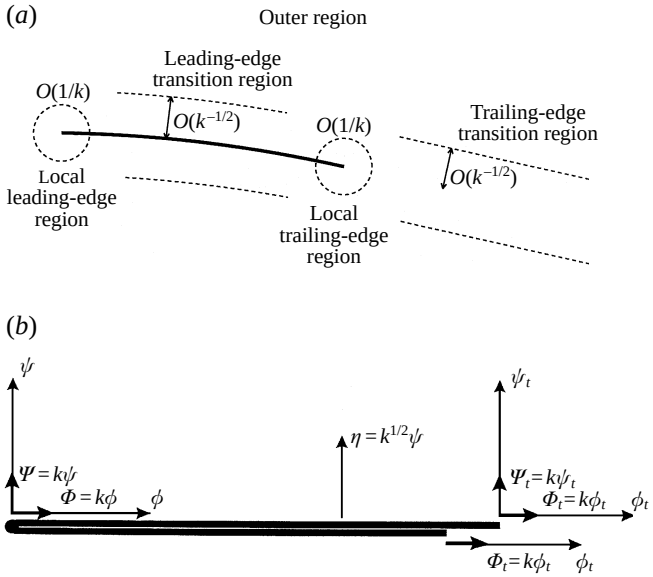

FIGURE 2. (*a*) Illustration of asymptotic regions in the physical plane, with sizes given in dimensionless coordinates. (*b*) Illustration of airfoil surface and coordinate systems in potential-streamfunction space.

into (2.9) and expanding for large k, we find

$$q - \mathrm{i}\mu = \frac{\alpha_{eff} k^{1/2}}{\beta_\infty} \sqrt{2} (\Phi + \mathrm{i}\Psi)^{-1/2} + O(\alpha, \alpha^2 k), \tag{3.2}$$

where

$$\alpha_{eff} = \alpha_i - \alpha_{1c}, \tag{3.3a}$$

and

$$\alpha_{1c} = \frac{1}{\pi} \int_0^2 \frac{(1-s) n(s) \mathrm{d}s}{[s(2-s)]^{3/2}}. \tag{3.3b}$$

Equation (3.2) describes an inverse-square-root flow around the sharp leading edge, identical to that for a flat plate but with a modified strength, α_{eff}. The parameter α_{eff} will later be shown to be a dominant correlating parameter for the sound power level.

The source terms in the equations governing the unsteady disturbance in the local leading-edge region contain the local expansions of the flow speed q and conjugate function μ, and the local expansion of the drift function g. As for the flat-plate airfoil, the drift function vanishes to $O(\alpha)$ at the leading edge of a cambered airfoil. The local expansions for q, μ, and g are then identical to the expressions derived previously for a flat-plate airfoil, except that α is replaced by α_{eff}. Therefore the $\alpha k^{1/2} \ll 1$ solution for the modified potential $H(\Phi, \Psi)$ in the local leading-edge region derived in MK95 applies here as well, when α in MK95 is replaced by α_{eff}. By expressing $H(\Phi, \Psi)$ in outer coordinates and expanding for large k, we obtain an asymptotic matching condition for the leading-edge behaviour of the geometric-acoustic field for the outer region,

$$h \sim \left[D_0(\theta) \left(1 + \alpha_{eff} k^{1/2} \left(-2\mathrm{i}\beta_\infty w + \frac{\mathrm{i}(\gamma+1) M_\infty^4 (\delta - w\cos\theta)^2}{\beta_\infty^3 w} \right) (2kr)^{1/2} \cos\tfrac{1}{2}\theta \right) \right.$$

$$+\alpha_{eff}k^{1/2}\left(D_1(\theta)+D_2(\theta)+D_3(\theta)\right)\Big]\frac{e^{ikwr}}{(kr)^{1/2}}+0(k^{-3/2},\alpha k^{-1/2}), \quad (3.4)$$

where (r,θ) is the polar form of (ϕ,ψ) and D_0, D_1, D_2 and D_3 are the directivity functions defined in (3.8*b*), (3.11*b*), (3.15*e*), and (3.26*c*) of MK95. The directivity functions are repeated for convenience in the Appendix. The term containing α_{eff} which multiplies D_0 is a secular term arising in the analysis of the local leading-edge region; this term matches with the phase distortion σ_{1l} (defined below) of the geometric-acoustic field in the outer region. The directivity functions $D_i(\theta)$ are used to specify the amplitude of the geometric-acoustic field. From (3.4) it can be seen that effects due to camber enter the local leading-edge region in a simple way, through the single parameter α_{eff}.

4. Outer region

The analysis of MK95 shows that the solution in the outer region contains four components: a particular solution h_p that accounts for the volume-source term in (2.3*a*), a complementary solution h_c required to cancel the gust upwash (2.6) through the airfoil surface, and ray-acoustic fields h_l and h_t that emanate from the local regions at the leading and trailing edges of the airfoil. The components h_p and h_c are unrelated to the sound field and were discussed in MK95. Here, we present results for the leading- and trailing-edge ray fields.

In MK95, it was shown that the geometric-acoustic field emanating from the leading edge can be written in a general form, in terms of the $O(\alpha)$ perturbation flow speed q which characterizes the spatial variations of the medium, as

$$h_l = k^{-3/2}A_l(r,\theta)e^{ik\sigma_l}+O(\alpha k^{-3/2},k^{-5/2}), \quad (4.1a)$$

where

$$\sigma_l = wr+\sigma_{1l}(r,\theta)+O(\alpha^2), \quad (4.1b)$$

$$\sigma_{1l} = V(\theta)\int_0^r q(r',\theta)dr', \quad (4.1c)$$

$$V(\theta) = -\beta_\infty^2 w+\frac{(\gamma+1)M_\infty^4}{2\beta_\infty^2 w}(\delta-w\cos\theta)^2, \quad (4.1d)$$

and A_l is determined through asymptotic matching with the local leading-edge region. The $O(\alpha)$ phase distortion σ_{1l} can be written in terms of the perturbation complex potential:

$$\sigma_{1l} = V(\theta)\mathrm{Re}\left\{e^{-i\theta}F(re^{i\theta})\right\}. \quad (4.2)$$

The function F is given by (2.10)–(2.12) with the arbitrary constants C_i and C_c both set to -iπ, so that (4.2) vanishes at the airfoil leading edge. The asymptotic expansion of (4.2) for large r, required for determination of the far-field sound, is

$$\sigma_{1l}\sim\frac{V\theta}{\beta_\infty}\left[\alpha_g\sin\theta\log 2r-\alpha_g(\theta-\pi)\cos\theta+(\alpha_i-\alpha_{3c})\sin\theta\right]+O(\alpha/r), \quad (4.3a)$$

where θ lies in the range $0\leqslant\theta\leqslant 2\pi$,

$$\alpha_g = \alpha_i+\alpha_{2c}, \quad (4.3b)$$

$$\alpha_{2c} = \frac{1}{\pi}\int_0^2\frac{n(s)ds}{s^{1/2}(2-s)^{3/2}}, \quad (4.3c)$$

and

$$\alpha_{3c} = \frac{1}{\pi}\int_0^2 \frac{n(s)\mathrm{d}s}{(s(2-s))^{1/2}}. \tag{4.3d}$$

The only numerical integrations required to determine the phase distortion of the far-field sound are those defining α_{2c} and α_{3c}.

The matching procedure which determines the amplitude function $A_l(r,\theta)$ is nearly identical to the procedure described in MK95 for the flat-plate airfoil. Upon repeating that procedure we find that the amplitude is given by the local leading-edge directivity series with a cylindrical-wave decay:

$$A_l(r,\theta) = r^{-1/2}D_l(\theta), \tag{4.4a}$$

where

$$D_l(\theta) \equiv \left[D_0(\theta) + \alpha_{eff}k^{1/2}(D_1(\theta) + D_2(\theta) + D_3(\theta))\right], \tag{4.4b}$$

with the functions D_i given in (3.4).

The geometric-acoustic field emanating from the trailing edge has a similar form,

$$h_t = k^{-2}A_t(r_t,\theta_t)\mathrm{e}^{\mathrm{i}k\sigma_t} + O(\alpha k^{-2}, k^{-3}), \tag{4.5}$$

where the trailing-edge coordinate system (r_t,θ_t) is described in §6. The trailing-edge phase function is given by

$$\sigma_t = wr_t + \sigma_{1t}(r_t,\theta_t) + O(\alpha^2), \tag{4.6a}$$

$$\sigma_{1t} = (-\beta_\infty^2 w + \frac{(\gamma+1)M_\infty^4}{2\beta_\infty^2 w}(\delta - w\cos\theta_t)^2)\int_0^{r_t} q_t(r_t',\theta_t)\mathrm{d}r_t' \tag{4.6b}$$

$$= V(\theta_t)\mathrm{Re}\left\{\mathrm{e}^{-\mathrm{i}\theta_t}F_t(r_t\mathrm{e}^{\mathrm{i}\theta_t})\right\}. \tag{4.6c}$$

Here q_t and F_t are the flow speed q and complex potential F with the leading-edge coordinates expressed in terms of trailing-edge coordinates, and the arbitrary constants C_i and C_c are set to -2 and 0 respectively so that F_t vanishes at the trailing edge. The asymptotic expansion of σ_{1t} for large r_t is

$$\sigma_{1t}(\theta_t) \sim \frac{V(\theta_t)}{\beta_\infty}\left[\alpha_g\sin\theta_t\log 2r_t - \alpha_g\theta_t\cos\theta_t - (\alpha_i+\alpha_{3c})\sin\theta_t\right] + O(\alpha/r_t), \tag{4.7}$$

where θ_t lies in the range $-\pi \leqslant \theta_t \leqslant \pi$. The trailing-edge amplitude function A_t is determined by matching with the local trailing-edge region, which is discussed in §6.

5. Leading-edge transition region

In the geometric-acoustic approximation employed in the outer region, information travels along rays emanating from the airfoil edges. Hence the boundary condition along the airfoil surface away from the edges cannot be incorporated directly into the geometric-acoustic solution. For a flat-plate airfoil the leading-edge ray field satisfies the homogeneous form of the boundary condition (2.6), because the airfoil maintains the shape assumed in the leading-edge region throughout its length. For a cambered airfoil, however, the shape changes along the length, and it is thus not surprising that the leading-edge ray field yields a non-zero normal-velocity component on the airfoil surface. Differentiation of (4.1) with respect to ψ gives

$$\left.\frac{\partial h_l}{\partial\psi}\right|_{\psi=0^\pm} = \frac{\mathrm{i}D_l(0,2\pi)V(0)}{k^{1/2}\phi^{3/2}}\int_0^\phi \phi'\frac{\partial q}{\partial\psi}(\phi',0)\mathrm{d}\phi'\mathrm{e}^{\mathrm{i}k\sigma_l(r=\phi,\theta=0,2\pi)} + O(\alpha/k). \tag{5.1a}$$

The notation $D_l(0, 2\pi)$ implies that the directivity function $D_l(\theta)$ is to be evaluated at $\theta = 0$ for the upper surface of the airfoil ($\psi = 0^+$) and $\theta = 2\pi$ for the lower surface. Likewise, the value of θ in σ_l (given in (4.1)) is 0 on the airfoil upper surface and 2π on the lower surface. By using the Cauchy–Riemann conditions to relate the ψ-derivative of the perturbation speed q to the ϕ-derivative of its conjugate harmonic μ, and using the mean-flow boundary condition to equate $\beta_\infty \mu$ to the body slope, we find that (5.1a) may be rewritten in terms of the camber distribution function $n(x)$ as

$$\left.\frac{\partial h_l}{\partial \psi}\right|_{\psi=0^\pm} = \frac{\mathrm{i}D_l(0,2\pi)V(0)}{k^{1/2}\phi^{3/2}\beta_\infty}\left[\phi n'(\phi) - n(\phi)\right]\mathrm{e}^{\mathrm{i}k\sigma_l(r=\phi,\theta=0,2\pi)}. \tag{5.1b}$$

The quantity in square brackets may be recast (using Taylor's theorem with $n(0) = 0$) as $|n''(\phi_a)|\phi^2/2, 0 < \phi_a < \phi$, and thus represents an average curvature of the airfoil segment between the leading edge and the point ϕ. Modifications to the flat-plate theory must be made to account for the finite radius of curvature of the airfoil.

The curvature effects are accounted for by introducing an acoustic boundary layer of extent $\psi = O(k^{-1/2})$, in which the modified potential satisfies a parabolic differential equation. (The Reynolds number is assumed large so that the viscous boundary layer is thin compared to this acoustic boundary layer and can be ignored in our analysis.) The acoustic boundary layer is similar in form to the transition region introduced (MK95) downstream of the trailing edge of the flat-plate airfoil; the solutions in the two regions exhibit similar combinations of ray-field and diffracted-field characteristics. The transition region accounting for the airfoil surface curvature will be labelled the 'leading-edge transition region', since it extends from the leading edge, while the downstream transition region will be relabelled the 'trailing-edge transition region'.

The leading-edge transition field is a scattered solution which serves to correct the boundary condition on the airfoil surface, and decays to zero for large values of ψ, where a purely geometric description is appropriate. We proceed by introducing the scaled variable

$$\eta = k^{1/2}\psi \tag{5.2}$$

and attempting a scattered solution of the form (the subscript *ltn* signifying 'leading-edge transition')

$$h_{ltn} = \frac{1}{k}J_l(\phi,\eta)\mathrm{e}^{\mathrm{i}k\sigma_l(r=\phi,\theta=0,2\pi)} + O(\alpha/k^{3/2}), \tag{5.3}$$

where the function J_l is $O(\alpha)$. Upon inserting (5.2) and (5.3) into the homogeneous form of (2.3a), we find that to leading order $J_l(\phi, \eta)$ satisfies

$$2\mathrm{i}w\frac{\partial J_l}{\partial \phi} + \frac{\partial^2 J_l}{\partial \eta^2} = 0. \tag{5.4}$$

The scattered solution must cancel the normal velocity (5.1) on the airfoil surface. In addition, it is advantageous to extend the boundary condition into the wake in a manner which simplifies the analysis of the local trailing-edge and trailing-edge transition fields (by obviating the need for a complementary solution to satisfy the velocity jump condition across the wake). We write the airfoil boundary condition and its extension in the following way:

$$\left.\frac{\partial J_l}{\partial \eta}\right|_{\eta=0^\pm} = K_\pm(\phi), \tag{5.5a}$$

where

$$K_{\pm}(\phi) = \begin{cases} -\mathrm{i}\dfrac{D_l(0,2\pi)V(0)}{\phi^{3/2}}\displaystyle\int_0^{\phi}\phi'\frac{\partial q}{\partial \psi}(\phi',0)\mathrm{d}\phi', \ 0 \leqslant \phi \leqslant 2 \\ -\mathrm{i}\dfrac{D_l(0,2\pi)V(0)}{\phi^{3/2}}\displaystyle\int_0^{2}\phi'\frac{\partial q}{\partial \psi}(\phi',0)\mathrm{d}\phi', \ \phi > 2. \end{cases} \tag{5.5b}$$

A solution for $J_l(\phi,\eta)$ may be obtained by applying a cosine transform in η to (5.4), incorporating (5.5*a*), and requiring that $J_l \to 0$ as $\eta \to \pm\infty$. After solving the resulting first-order differential equation in ϕ in terms of a definite integral, then switching the order of integration and evaluating the integral defining the transform inversion, we find that

$$J_l(\phi,\eta) = -\mathrm{sgn}(\eta)\frac{\mathrm{e}^{\mathrm{i}\pi/4}}{(2\pi w)^{1/2}}\int_0^{\phi}\mathrm{e}^{\mathrm{i}w\eta^2/2(\phi-\xi)}\frac{K_{\pm}(\xi)}{(\phi-\xi)^{1/2}}\mathrm{d}\xi. \tag{5.6}$$

When (5.5*b*) is inserted explicitly into (5.6), the resulting integrals can be written partially in terms of a complementary error function. The total solution (5.3) becomes (for $\phi > 2$)

$$h_{ltn} = \frac{\mathrm{sgn}(\psi)}{k}\mathrm{e}^{\mathrm{i}k\sigma_l(r=\phi,\theta=0,2\pi)}\frac{\mathrm{e}^{3\mathrm{i}\pi/4}V(0)D_l(0,2\pi)}{(2\pi w)^{1/2}\beta_{\infty}}\left\{\int_0^{2}\frac{\mathrm{e}^{\mathrm{i}w\eta^2/2(\phi-\xi)}(\xi n'(\xi)-n(\xi))}{(\phi-\xi)^{1/2}\xi^{3/2}}\mathrm{d}\xi\right.$$

$$\left.+2^{3/2}n'(2)\left(\frac{\mathrm{e}^{\mathrm{i}w\eta^2/2(\phi-2)}(\phi-2)^{1/2}}{\phi} - \frac{|\eta|e^{-\mathrm{i}\pi/4}(\pi w)^{1/2}\mathrm{e}^{\mathrm{i}w\eta^2/2\phi}}{\phi^{3/2}}\mathrm{erfc}\left[\frac{\mathrm{e}^{-\mathrm{i}\pi/4}w^{1/2}|\eta|}{(\phi(\phi-2))^{1/2}}\right]\right)\right\} \tag{5.7}$$

(For $\phi < 2$, the terms multiplying $n'(2)$ vanish, and the upper limit on the ξ-integral changes from 2 to ϕ.) The large-r asymptotic expansion of (5.7), valid for all polar angles θ, is given by

$$h_{ltn} \sim \frac{1}{k}D_{ltn}(\theta)\frac{\mathrm{e}^{\mathrm{i}k\sigma_l(r,\theta)}}{r^{1/2}}, \tag{5.8a}$$

where

$$D_{ltn}(\theta) = \mathrm{sgn}(\psi)\frac{\mathrm{e}^{3\mathrm{i}\pi/4}V(0)D_l(0,2\pi)}{(2w\pi)^{1/2}\beta_{\infty}}\left\{\int_0^{2}\frac{\mathrm{e}^{\mathrm{i}kw(1-\cos\theta)\xi}(\xi n'(\xi)-n(\xi))}{\xi^{3/2}}\mathrm{d}\xi\right.$$

$$\left.+2^{3/2}n'(2)\left(\mathrm{e}^{2\mathrm{i}kw(1-\cos\theta)} - \pi^{1/2}\mathrm{e}^{-\mathrm{i}\pi/4}(2kw(1-\cos\theta))^{1/2}\mathrm{erfc}(\mathrm{e}^{-\mathrm{i}\pi/4}(2kw(1-\cos\theta))^{1/2})\right)\right\}. \tag{5.8b}$$

The leading-edge transition field has been derived in this section for the specific case of diffraction by the curved airfoil surface, but the general approach is more widely applicable. Myers & Kerschen (1992) present a higher-order perturbation expansion for the transition solution in the case of a stratified medium, and show how this solution can be used to account for diffraction of a general source field by either a curved surface or gradients of the acoustic medium.

6. Local trailing-edge region

To analyse the acoustic field in the local trailing-edge region, it is first necessary to determine the location of the trailing edge in (ϕ,ψ)-space. To do so we use the relation

$$\zeta = z + F(z) + O(\alpha^2), \tag{6.1}$$

where $\zeta = \phi + \mathrm{i}\psi$ and $z = x_1 + \mathrm{i}\beta_\infty x_2$. Here F is the total $O(\alpha)$ perturbation potential F, given in (2.10) (with the arbitrary constants chosen so that F vanishes at the leading edge.) By inserting $z = 2$ in (2.10), we find that the trailing-edge location is given by $\phi = 2 \pm \pi\alpha_g/\beta_\infty + O(\alpha^2)$, where α_g is defined in (4.3) and the plus and minus signs apply on the airfoil upper ($\psi = 0^+$) and lower ($\psi = 0^-$) surfaces, respectively. The parameter $\pi\alpha_g/\beta_\infty$ is one-half the non-dimensional circulation around the airfoil, so that the lift coefficient $C_L = 2\pi\alpha_g/\beta_\infty$. To analyse trailing-edge effects, we define trailing-edge-based coordinates for the outer region:

$$\phi_t = \phi - (2 \pm \pi\alpha_g/\beta_\infty), \quad \psi_t = \psi, \tag{6.2}$$

where the plus and minus signs apply for ψ greater than and less than zero, respectively. The $O(\alpha)$ contribution to the trailing-edge location leads to an $O(1)$ phase shift that must be included when considering the scattering by the trailing edge.

The interaction of the convected disturbance with the trailing edge, which does not contribute to the sound field, is discussed in MK95. Here, we consider only the scattering of the leading-edge ray and transition fields by the trailing edge. To analyse this scattering, local trailing-edge coordinates

$$\Phi_t = k\phi_t, \quad \Psi_t = k\psi_t \tag{6.3}$$

are introduced. In the local trailing-edge region, mean-flow gradients are $O(\alpha)$ and hence too small to enter the analysis. Thus, the modified potential $H_t(\Phi_t, \psi_t)$ satisfies a constant-coefficient Helmholtz equation. Behind the airfoil ($\Phi_t > 0$), the function H_t must cancel the jump in pressure across $\Psi_t = 0$ of the leading-edge ray field and the leading-edge transition field. Applying the pressure operator (2.7*b*) to (4.1) and (5.3) and expanding in local trailing-edge coordinates, the combined jump in pressure due to h_l and h_{ltn} is found to be

$$p\left|\begin{array}{l}\Psi_t = 0^+ \\ \Psi_t = 0^-\end{array}\right. = \frac{\Delta}{k^{1/2}} \mathrm{e}^{\mathrm{i}(w - \delta M_\infty^2)\Phi_t}, \tag{6.4a}$$

where

$$\Delta = (P_+ - P_-) + k^{1/2}(P_+ + P_-)\frac{\mathrm{e}^{\mathrm{i}\pi/4}\mathrm{i}V(0)}{(\pi w)^{1/2}\beta_\infty}\int_0^2 \frac{\xi n'(\xi) - n(\xi)}{(2-\xi)^{1/2}\xi^{3/2}}\,\mathrm{d}\xi, \tag{6.4b}$$

$$P_+ = \frac{\mathrm{i}}{\sqrt{2}}(w - \delta)D_l(0)\mathrm{e}^{\mathrm{i}k\sigma_l(2 + \alpha_g\pi/\beta_\infty, 0)}\mathrm{e}^{-\mathrm{i}C_+}, \tag{6.4c}$$

$$P_- = \frac{\mathrm{i}}{\sqrt{2}}(w - \delta)D_l(2\pi)\mathrm{e}^{\mathrm{i}k\sigma_l(2 - \alpha_g\pi/\beta_\infty, 2\pi)}\mathrm{e}^{-\mathrm{i}C_-}, \tag{6.4d}$$

$$C_\pm = k\delta M_\infty^2(2 \pm \alpha_g\pi/\beta_\infty). \tag{6.4e}$$

The constant P_+ is the modified pressure (with the $1/k^{1/2}$ factored out) associated with the leading-edge ray field, evaluated on the upper surface at the trailing edge; P_- is the analogous pressure on the lower surface. The quantity $(P_+ - P_-)$, which was labelled Δ_p in the flat-plate analysis, therefore represents the pressure jump associated with the direct ray field h_l. The part of (6.4*b*) proportional to $(P_+ + P_-)$ represents the jump in modified pressure for the leading-edge transition field h_{ltn}, and is $O(\alpha k^{1/2})$ since the camber distribution function $n(x)$ is $O(\alpha)$.

The modified potential $H_t(\Phi_t, \Psi_t)$ in the local trailing-edge region then satisfies (3.46)–(3.48) of MK95, with the parameter Δ_p replaced by the more general parameter Δ and $C_\pm$ defined by (6.4*e*). The solution for $H_t(\Phi_t, \Psi_t)$ presented in MK95 then applies

here as well, and asymptotic matching with the trailing-edge ray field $h_t(r_t, \theta_t)$ for the outer region determines the amplitude function

$$A_t(r_t, \theta_t) = \frac{\mathrm{sgn}(\psi_t)\mathrm{e}^{-\mathrm{i}\pi 4}\Delta \mathrm{e}^{\mathrm{i}C_\pm}}{2\left[\pi w(1-\cos\theta_t)\right]^{1/2}(\delta - w\cos\theta_t)r_t^{1/2}}, \tag{6.5}$$

where (r_t, θ_t) is the polar form of (ϕ_t, ψ_t). Since the trailing-edge ray field (4.5) is multiplied by k^{-2}, and we neglect terms smaller than $O(1/k^2, \alpha k)$ in the outer region, the $O(\alpha k^{1/2})$ term in the definition of Δ (6.4*b*) can be neglected in (6.5). Thus, the scattering of the leading-edge transition field h_{ltn} does not contribute to the trailing-edge ray field at $O(1)$ values of θ_t, to the desired order of accuracy. However, for small values of θ_t the scattering of h_{ltn} by the trailing edge enters at $O(\alpha/k)$.

As in the flat-plate case, the trailing-edge amplitude function $A_t(r_t, \theta_t)$ is singular for small values of θ_t, indicating the need for a separate expansion in the trailing-edge transition region. This region is analysed in the next section.

7. Trailing-edge transition region

Like the local trailing-edge solution, the trailing-edge transition solution serves to cancel the jumps in pressure and transverse velocity across the wake ($\psi_t = 0$) introduced by the leading-edge ray field and the leading-edge transition field. In the local trailing-edge region, the abrupt change in boundary condition at the trailing edge was incorporated in the analysis, but the cylindrical decay of the leading-edge field was neglected. In contrast, the cylindrical decay of the leading-edge field must be accounted for in the trailing-edge transition region, but the boundary condition on the airfoil surface does not enter explicitly owing to the parabolic nature of the wave operator in this thin layer.

To construct the trailing-edge transition solution for an airfoil having both camber and angle of attack, we generalize the formulation of the trailing-edge transition solution for the flat plate. The solution will be obtained in terms of the general mean-flow perturbation speed expressed in trailing-edge coordinates, $q_t(\phi_t, \psi_t)$. We introduce the scaled coordinate

$$\eta = k^{1/2}\psi_t \tag{7.1}$$

and attempt a solution of the form (the subscript *ttn* signifying 'trailing-edge transition')

$$h_{ttn} = \frac{\mathrm{e}^{\mathrm{i}kw\phi_t}}{k^{3/2}}\left[J_{t0}(\phi_t, \eta) + k^{1/2}J_{t1}(\phi_t, \eta) + O(\alpha, 1/k, \alpha^2 k)\right], \tag{7.2}$$

which retains the phase dependence on the fast variable $k\phi_t$ and an amplitude dependence on the slow variable ϕ_t, but is also a function of the transverse coordinate η whose scale is intermediate between the fast and slow variables. The function J_{t0} is $O(1)$ while J_{t1} is $O(\alpha)$. The simple phase function $w\phi_t$ is adequate in (7.2) because, to $O(\alpha)$, q_t is zero along the wake line $\psi_t = 0$.

By using (7.1) and (7.2) in the homogeneous form of (2.3*a*), and imposing continuity of the total unsteady pressure and vertical velocity, we find at leading order that

$$2\mathrm{i}w\frac{\partial J_{t0}}{\partial \phi_t} + \frac{\partial^2 J_{t0}}{\partial \eta^2} = 0, \tag{7.3a}$$

$$\mathrm{e}^{-\mathrm{i}C_+}J_{t0}\Big|_{\eta=0^+} - \mathrm{e}^{-\mathrm{i}C_-}J_{t0}\Big|_{\eta=0^-} = \frac{\mathrm{i}(P_+ - P_-)}{w-\delta}\left(\frac{2}{2+\phi_t}\right)^{1/2}, \tag{7.3b}$$

$$\mathrm{e}^{-\mathrm{i}C_+}\frac{\partial J_{t0}}{\partial \eta}\bigg|_{\eta=0^+} - \mathrm{e}^{-\mathrm{i}C_-}\frac{\partial J_{t0}}{\partial \eta}\bigg|_{\eta=0^-} = 0. \tag{7.3c}$$

To within a multiplicative constant in (7.3*b*), this system of equations is identical to that for the flat-plate airfoil. We can thus immediately write the solution

$$J_{t0} = \frac{\mathrm{sgn}(\eta)\mathrm{i}(P_+ - P_-)\mathrm{e}^{\mathrm{i}C_\pm}}{(w-\delta)\sqrt{2}(2+\phi_t)^{1/2}}\mathrm{e}^{\mathrm{i}w\eta^2/2(2+\phi_t)}\mathrm{erfc}\left[\frac{\mathrm{e}^{-\mathrm{i}\pi/4}w^{1/2}|\eta|}{(\phi_t(2+\phi_t))^{1/2}}\right]. \tag{7.4}$$

It is convenient to break the $O(\alpha/k)$ term J_{t1} into two parts, one that cancels the discontinuity in vertical velocity across the wake and has zero pressure jump, and another whose vertical velocity across the wake is continuous but has the appropriate jump in pressure. Only the first type of solution, which we label $J_{t1,a}$, was required for the flat-plate airfoil. The governing equation for $J_{t1,a}$ is inhomogeneous, with the forcing term arising from the small-ψ_t expansion of the perturbation speed q appearing in the operator L_1 defined by (2.3*d*). We find that

$$2\mathrm{i}w\frac{\partial J_{t1,a}}{\partial \phi_t} + \frac{\partial^2 J_{t1,a}}{\partial \eta^2} = -2wV(0)\eta J_{t0}\frac{\partial q_t}{\partial \psi_t}(\phi_t, 0), \tag{7.5a}$$

$$\mathrm{e}^{-\mathrm{i}C_+}J_{t1,a}\bigg|_{\eta=0^+} - \mathrm{e}^{-\mathrm{i}C_-}J_{t1,a}\bigg|_{\eta=0^-} = 0, \tag{7.5b}$$

$$\mathrm{e}^{-\mathrm{i}C_+}\frac{\partial J_{t1,a}}{\partial \eta}\bigg|_{\eta=0^+} - \mathrm{e}^{-\mathrm{i}C_-}\frac{\partial J_{t1,a}}{\partial \eta}\bigg|_{\eta=0^-} = -\frac{V(0)(P_+ - P_-)\sqrt{2}}{w-\delta}$$

$$\times\left[(2+\phi_t)^{-1/2}\int_0^{\phi_t}\frac{\partial q_t}{\partial \psi_t}(\phi_t', 0)\mathrm{d}\phi_t' - (2+\phi_t)^{-3/2}\int_0^{\phi_t}\mathrm{d}\phi_t'\int_0^{\phi_t'}\frac{\partial q_t}{\partial \psi_t}(\phi_t'', 0)\mathrm{d}\phi_t''\right]. \tag{7.5c}$$

In the analysis for a flat-plate airfoil, the solution

$$J_{t1,a} = \mathrm{i}V(0)\eta J_{t0}\int_0^{\phi_t}\frac{\partial q_t}{\partial \psi_t}(\phi_t', 0)\mathrm{d}\phi_t' - \frac{V(0)}{w}\frac{\partial J_{t0}}{\partial \eta}\int_0^{\phi_t}\mathrm{d}\phi_t'\int_0^{\phi_t'}\frac{\partial q_t}{\partial \psi_t}(\phi_t'', 0)\mathrm{d}\phi_t'' \tag{7.6}$$

was derived using expressions for $\partial q_t/\partial \psi_t$ appropriate for a flat-plate airfoil. It can be verified by direct substitution that (7.6) provides the appropriate generalization for a cambered airfoil.

The second part of the $O(\alpha/k)$ term, $J_{t1,b}$, cancels the pressure jump across the wake created by the leading-edge transition solution (5.7). The system of equations satisfied by $J_{t1,b}$ is

$$2\mathrm{i}w\frac{\partial J_{t1,b}}{\partial \phi_t} + \frac{\partial^2 J_{t1,b}}{\partial \eta^2} = 0 \tag{7.7a}$$

$$\mathrm{e}^{-\mathrm{i}C_+}J_{t1,b}\bigg|_{\eta=0^+} - \mathrm{e}^{-\mathrm{i}C_-}J_{t1,b}\bigg|_{\eta=0^-} = -\frac{\mathrm{e}^{\mathrm{i}\pi/4}V(0)(P_+ + P_-)}{(w-\delta)(\pi w)^{1/2}\beta_\infty}b_t(\phi_t), \tag{7.7b}$$

$$\mathrm{e}^{-\mathrm{i}C_+}\frac{\partial J_{t1,b}}{\partial \eta}\bigg|_{\eta=0^+} - \mathrm{e}^{-\mathrm{i}C_-}\frac{\partial J_{t1,b}}{\partial \eta}\bigg|_{\eta=0^-} = 0 \tag{7.7c}$$

where

$$b_t(\phi_t) = \int_0^2 \frac{\xi n'(\xi) - n(\xi)}{(2+\phi_t-\xi)^{1/2}\xi^{3/2}}\mathrm{d}\xi + \frac{2^{3/2}n'(2)\phi_t^{1/2}}{2+\phi_t}. \tag{7.7d}$$

The alternative form

$$b_t(\phi_t) = \frac{2}{2+\phi_t}\int_0^2 (2+\phi_t-\xi)^{1/2}\xi^{1/2}n''(\xi)\mathrm{d}\xi \tag{7.7e}$$

is produced by integrating (7.7*d*) by parts.

A solution to (7.7) can be obtained using a cosine transform, in a manner similar to that used to derive (5.6) in the leading-edge transition region. The result is

$$J_{t1,b} = -\frac{\mathrm{e}^{\mathrm{i}C_\pm}V(0)(P_+ + P_-)}{(w-\delta)2^{3/2}\pi\beta_\infty}\int_0^{\phi_t}\frac{\eta b_t(v)}{(\phi_t - v)^{3/2}}\mathrm{e}^{\mathrm{i}w\eta^2/2(\phi_t - v)}\mathrm{d}v. \tag{7.8}$$

The matching of the trailing-edge transition solution with the local trailing-edge solution and the trailing-edge outer solution is similar to that in MK95. A uniformly valid trailing-edge outer solution is obtained by forming an additive composite of the trailing-edge outer and trailing-edge transition solutions. The common expansion is obtained by expressing the transition solution h_{ttn} to $O(\alpha/k)$ in outer variables and expanding to $O(\alpha/k, 1/k^2)$, or by expressing the outer ray solution (4.5) to $O(1/k^2)$ in transition variables and expanding to $O(\alpha/k)$. The two expansions are identical, verifying the asymptotic matching of these two regions. When expressed in transition variables the common expansion is

$$h_{com} = \frac{\mathrm{e}^{-\mathrm{i}\pi/4}(P_+ - P_-)\mathrm{e}^{\mathrm{i}C_\pm}\mathrm{e}^{\mathrm{i}kw\phi_t + \mathrm{i}w\eta^2/2\phi_t}\phi_t^{1/2}}{(2\pi w)^{1/2}(\delta - w)k^{3/2}\eta}\left[1 + \frac{\mathrm{i}k^{1/2}\eta V(0)}{\phi_t}\int_0^{\phi_t}\phi_t'\frac{\partial q_t}{\partial \psi_t}(\phi_t', 0)\mathrm{d}\phi_t'\right]. \tag{7.9}$$

The transition solution $J_{t1,b}$ does not contribute to the common expansion. Like the leading-edge transition solution J_l that is generated by surface-curvature effects, this solution becomes negligibly small in the outer region.

The uniformly valid trailing-edge outer solution $h_{t,u}$ is the trailing-edge ray field plus the transition field minus the common part:

$$h_{t,u} = h_t + h_{ttn} - h_{com}. \tag{7.10}$$

The large-r expansion of $h_{t,u}$ is

$$h_{t,u} \sim \frac{1}{k^{3/2}}D_{t,u}(\theta_t)\mathrm{e}^{\mathrm{i}k\sigma_t(r_t,\theta_t)}, \tag{7.11a}$$

where

$$\begin{aligned} D_{t,u}(\theta_t) = \frac{\mathrm{e}^{\mathrm{i}C_\pm}}{\sqrt{2}(\delta - w\cos\theta_t)}\Bigg\{ & -\mathrm{sgn}(\psi_t)\mathrm{i}(P_+ - P_-)\mathrm{e}^{-2\mathrm{i}kw(1-\cos\theta_t)} \\ & \times \mathrm{erfc}\left(\mathrm{e}^{-\mathrm{i}\pi/4}(2kw(1-\cos\theta_t))^{1/2}\right) - \frac{2k^{1/2}V(0)(\alpha_i - n'(2))(P_+ - P_-)\mathrm{e}^{\mathrm{i}\pi/4}}{(\pi w)^{1/2}\beta_\infty} \\ & \times\left(1 - \pi^{1/2}\mathrm{e}^{-\mathrm{i}\pi/4}(2kw(1-\cos\theta_t))^{1/2}\mathrm{e}^{-2\mathrm{i}kw(1-\cos\theta_t)}\mathrm{erfc}\left(\mathrm{e}^{-\mathrm{i}\pi/4}(2kw(1-\cos\theta_t))^{1/2}\right)\right) \\ & + \frac{k^{1/2}\mathrm{sgn}(\psi_t)V(0)(P_+ + P_-)}{(2w)^{1/2}\pi\beta_\infty}(kw(1-\cos\theta_t))^{1/2}\int_0^\infty \mathrm{e}^{\mathrm{i}kw(1-\cos\theta_t)\xi}b_t(\xi)\mathrm{d}\xi\Bigg\}. \end{aligned} \tag{7.11b}$$

8. Total far-field solution

We now combine the solutions to the convected wave equation (2.3) into an expression for the total acoustic field in the geometric far field, $r \gg 1$. The trailing-

edge coordinates are expressed in terms of the leading-edge coordinates via the far-field transformations

$$r_t = r - (2 + \mathrm{sgn}(\psi)\alpha_g \pi/\beta_\infty)\cos\theta + O(1/r), \tag{8.1a}$$

$$\theta_t = \theta - [1 - \mathrm{sgn}(\psi)]\,\pi + O(1/r), \tag{8.1b}$$

where $0 \leqslant \theta \leqslant 2\pi$ and the $\mathrm{sgn}(\psi)$ is required due to the different range of θ_t. The total solution is the sum of the leading-edge ray field (4.1), the leading-edge transition field (5.8), and the uniform trailing-edge solution (7.10). For $r \gg 1$ this sum may be written

$$\begin{aligned} h_{total} \sim & \frac{\exp\left(\mathrm{i}k\left[wr + \dfrac{V(\theta)}{\beta_\infty}((\alpha_g \log 2r - \alpha_{3c})\sin\theta - \alpha_g(\theta-\pi)\cos\theta)\right]\right)}{k^{3/2}r^{1/2}} \\ & \times\left\{\exp\left(\mathrm{i}kV(\theta)\frac{\alpha_i}{\beta_\infty}\sin\theta\right)\left[D_l(\theta) + k^{1/2}D_{ltn}(\theta)\right]\right. \\ & \left.+\exp\left(\mathrm{i}k\left(-2w\cos\theta - \mathrm{sgn}(\psi)\pi\frac{\alpha_g}{\beta_\infty}(w + V(\theta))\cos\theta - \frac{\alpha_i}{\beta_\infty}V(\theta)\sin\theta\right)\right)D_{t,u}(\theta)\right\}, \end{aligned} \tag{8.2}$$

where the directivities D_l, D_{ltn}, and $D_{t,u}$ are defined in (4.4), (5.8*b*), and (7.11*b*), respectively, and the phase function $V(\theta)$ is given by (4.1*d*).

The far-field form of the modified pressure (2.7*b*) is

$$p_{total} = -\mathrm{i}k(\delta - w\,\cos\theta)\mathrm{e}^{-\mathrm{i}k\delta M_\infty^2 r\,\cos\theta}h_{total}. \tag{8.3}$$

The total far-field solutions just presented are given in terms of the potential-streamline coordinates (r,θ). The relations between (r,θ) and physical coordinates (r_{ph},θ_{ph}) (where r_{ph} is scaled by the airfoil semi-chord b) are

$$\tan\theta = \beta_\infty\,\tan\theta_{ph} \tag{8.4a}$$

and

$$\begin{aligned} r = (1 - M_\infty^2\,\sin^2\theta_{ph})^{1/2}r_{ph} + \frac{\alpha_g}{\beta_\infty}\left(\log[2(1 - M_\infty^2\,\sin^2\theta_{ph})^{1/2}r_{ph}]\,\sin\theta - (\theta-\pi)\,\cos\theta\right) \\ + \frac{\alpha_i - \alpha_{3c}}{\beta_\infty}\sin\theta. \end{aligned} \tag{8.4b}$$

The $O(\alpha)$ terms in (8.4*b*) were erroneously omitted from the corresponding expression (equation (4.2)) in MK95. However, the omitted terms provide only a phase shift to the total solution (see (8.2)), and do not affect calculations of acoustic power or pressure magnitude.

9. Results and discussion

9.1. *Summary of solution structure*

The following physical picture emerges from the analysis. For short-wavelength gusts, the primary sound generation is concentrated in the local leading-edge region. In this region the lengthscale of the mean-flow gradients is the same as the wavelength, so that the gust is distorted 'rapidly'. Sound is generated by interaction of the gust

with the airfoil surface, by interaction of the gust with mean-flow gradients, and by scattering effects due to sound propagation through the locally non-uniform mean flow. In contrast, the lengthscale for the mean-flow gradients in the outer region is the airfoil chord, so that the gust distortion is 'slow' and does not generate additional sound. However, as the sound which was generated in the local leading-edge region propagates through the outer region as a ray field, it undergoes $O(1)$ phase shifts due to the mean-flow variations. Two rays propagate along the upper and lower surfaces of the airfoil, with some modifications due to the surface curvature, and are then scattered by the trailing edge. The far-field sound is a combination of the direct rays from the leading edge and the scattered rays from the trailing edge. At shallow angles, the far field exhibits diffraction characteristics related to propagation along the curved surfaces of the airfoil and to the shadow boundaries of the trailing edge.

Except at shallow angles, the effect of airfoil camber enters the far-field expression (8.2) for the acoustic field in a simple manner, through the parameters α_{eff} and α_g. The incidence angle α_i of the airfoil also enters (8.2) through the parameters α_{eff} and α_g, and appears separately in the phases of the leading- and trailing-edge fields as well, influencing the constructive/destructive interference between these ray fields. An additional camber parameter, α_3, affects only the phase of the combined far field and thus is much less important. Both α_{eff} and α_g are given in terms of integrals of the camber distribution, which need be calculated only once to determine the far-field sound at any location outside the transition region. The physical interpretation of these generalized parameters is discussed below. The relative importance of α_{eff} and α_g on the total sound field will be quantitatively explored in §9.2.2.

The parameter α_{eff} is related to the mean flow in the local leading-edge region. In this region, the mean flow consists of a uniform flow parallel to the edge, plus a disturbance flow around the edge from the lower surface to the upper. The parameter α_{eff} is a measure of the relative amplitude of this disturbance flow. Physically, α_{eff} is the incidence angle which would be required for a flat-plate airfoil in order to produce the same amplitude disturbance flow around the leading edge. Thus, $\alpha_{eff} = \alpha_i - \alpha_{1c}$ can be thought of as an 'effective leading-edge incidence angle' for the cambered airfoil. The camber term α_{1c} (defined by (3.3*b*)) is zero for airfoils which are symmetric about the midchord, such as a circular arc. For most airfoils the maximum in the camber distribution occurs before the midchord, and α_{1c} is positive. Positive α_{1c} implies a camber-induced disturbance flow around the leading edge from the upper surface to the lower (assuming the airfoil to be concave down), the opposite direction to that induced by a positive incidence angle. Typically, then, airfoil camber and incidence angle oppose one another in the determination of α_{eff} and hence in the amplitude of the far-field sound.

Because the geometry and flow field in the local leading-edge region are the same as those for the flat-plate airfoil once the incidence angle is replaced by α_{eff}, the sound-generation mechanisms in the general case are identical to those for the flat plate. The weighting of the source terms related to non-uniform mean-flow effects merely changes from $\alpha_i k^{1/2}$ to $\alpha_{eff} k^{1/2}$. The sound-generation mechanisms are contained in the leading-edge potentials H_1, H_2, and H_3 of MK95, which are represented in the far field by the directivity patterns $D_1(\theta)$, $D_2(\theta)$, and $D_3(\theta)$ in (3.4). The function H_1 is generated by sources on the airfoil surface which arise from the change in boundary condition due to distortion of the vortical gust by the mean-flow gradients. H_2 is due to the volume sources arising from the interaction of the vortical velocity with the mean-flow gradients. Distortion of the entropy disturbance also contributes to H_2. The function H_3 represents additional sound generated by local scattering of the

uniform-medium sound field (represented by H_0) by local variations in the mean-flow velocity and speed of sound.

The parameter $\alpha_g = \alpha_i + \alpha_{2c}$ arises in the expression for the generalized geometric-acoustic phases. We refer to α_g as the 'total loading' parameter, since the airfoil mean lift coefficient is $C_L = 2\pi\alpha_g/\beta_\infty$. The typical situation which generates opposing influences of camber and incidence angle for α_{eff} produces complementary influences for α_g. The camber contribution to the total loading, α_{2c}, can be seen from (4.3*c*) to be always positive (for the airfoil concave down), thereby producing the same effect as a positive incidence angle. The airfoil total loading leads to a logarithmic contribution to the far-field phase, as can be seen from (8.2) and (8.4). The total loading also has a major impact on the scattered field from the trailing edge, as discussed next.

For a flat-plate airfoil at zero incidence angle, the leading-edge sound field is antisymmetric in ψ, and the pressure fluctuations that impinge on the upper and lower surfaces of the trailing edge are of equal amplitude but opposite phase. When the effects of airfoil camber and incidence angle are included, the radiation impinging on the upper and lower surfaces of the trailing edge is in general different in amplitude ($D_l(2\pi) \neq D_l(0)$), and has also suffered different $O(1)$ phase shifts in propagating from the leading to the trailing edge. For a two-dimensional gust ($A_3 = k_3 = 0$ in (2.1*a*)), the leading-edge rays which impinge on the upper and lower surfaces of the trailing edge have the phases

$$2k\frac{M_\infty}{1+M_\infty} \mp k\alpha_g \frac{\pi}{\beta_\infty}\frac{M_\infty^2}{(1+M_\infty)^2}\left[1 - \tfrac{1}{2}(\gamma-1)M_\infty\right], \tag{9.1}$$

where account has been taken of the additional phase factor that was extracted from the modified potential h in the definition (2.2) (see also Kerschen & Myers 1987). The phase shifts on the upper and lower surfaces due to the non-uniform mean-flow effects are seen to be of equal amplitude but opposite sign, and depend on the airfoil camber and incidence angle only through the total loading parameter α_g. These phase shifts may decrease the discontinuity Δ of the leading-edge pressure field at the trailing edge, in which case the airfoil mean loading weakens the scattered field from the trailing edge by an $O(1)$ amount.

At shallow angles ($\theta = O(k^{1/2})$) the geometric acoustic fields give way to transition solutions, which maintain the rapidly varying phase of geometric acoustics but acquire a dependence on the intermediate variable $k^{1/2}\theta$. Part of the trailing-edge transition solution h_{ttn} arises due to diffraction of the leading-edge field by the semi-infinite wake sheet, which is geometrically a plane in (ϕ, ψ)-space. This part of the solution also occurs for a flat-plate airfoil, and can be obtained from the flat-plate result simply by replacing the trailing-edge pressure jump of the leading-edge geometric field by the generalized pressure jump $P_+ - P_-$.

The remainder of the field at shallow angles is due specifically to the curvature of the airfoil surface. The solution h_{ltn} describes the acoustic field near the curved surface: above the airfoil it can be thought of as a boundary-layer extending slightly into the shadow region produced by the convex surface, while below the airfoil an enhancement of the acoustic field related to the whispering-gallery phenomenon is found. The boundary-layer approach is valid because the radius of curvature of the airfoil surface is large relative to the propagation distance (the airfoil chord.) The dependence upon airfoil camber in the transition solutions is more complicated than in the solutions previously discussed. Both h_{ltn} and h_{ttn} contain integrals over distributions of sources along the airfoil chord. The source strength is related to the local radius of curvature of the airfoil, as can be seen in (5.8) and (7.7*d*). To obtain

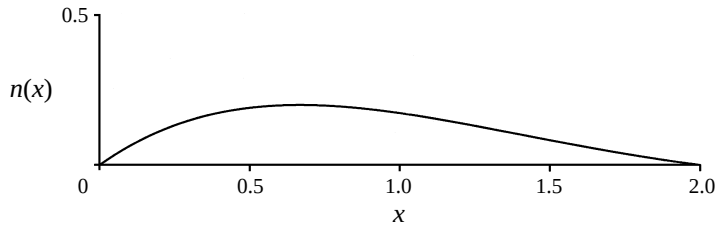

FIGURE 3. 10–33 airfoil, which attain maximum camber of 10% at 33% chord.

the far-field sound at shallow angles, it is necessary to calculate the integrals over airfoil source distributions for each receiver angle of interest.

9.2. *Numerical results*

Numerical calculations were performed to assess the influences of the various parameters characterizing the mean flow and the convected disturbance. Owing to the large dimension of the parameter space, several parameters are eliminated from consideration here. Only two-dimensional gusts are considered ($A_3 = k_3 = 0$) and the gusts are purely vortical except where a non-zero value of the entropy amplitude B is specified. Fixing $|\boldsymbol{A}| = 1$, the gust is then described by its orientation angle θ_g (the angle between the gust wavevector and the mean velocity far upstream) and the dimensionless frequency k.

The camber distribution function was varied by prescribing it in the form of the quartic polynomial

$$n(x) = a_0(1 + a_1x + a_2x^2)(1 - (1 - x)^2), \quad 0 \leqslant x \leqslant 2, \tag{9.2}$$

and varying the coefficients a_0, a_1, and a_2. The quartic polynomial representation provides considerable flexibility in specifying the airfoil shape, and also allows the integrals in the far-field forms of the transition solutions to be written in terms of complementary error functions. Two specific camber distribution functions will primarily be considered in this paper. The first, which results from the choices $a_1 = -0.61$ and $a_2 = 0.1$ in (9.2), attains its maximum at 33% chord and has an inflection point at 70% chord. It will be designated as the 'X-33' airfoil, where 'X' is the maximum percent camber (normalized by airfoil chord), which determines the final coefficient a_0. A 10-33 airfoil is shown in figure 3. The second type of airfoil considered is the circular arc, whose camber distribution function results from setting $a_1 = a_2 = 0$ in (9.2). The two airfoil shapes were chosen because the maxima in their camber distribution functions occur in distinct locations, resulting in significantly different values (between the two shapes) for both of the loading parameters α_{eff} and α_g.

Details of the acoustic field will be illustrated through plots of pressure directivity. The pressure directivity which we plot is the far-field value of $|p|r_{ph}^{1/2}$ as a function of θ_{ph} (see figure 4*a*), where p is the modified pressure defined by (8.3) and (2.7), and (r_{ph}, θ_{ph}) are polar coordinates in physical space. The far-field relations between the Prandtl–Glauert potential-streamline coordinates used throughout the analysis and the physical coordinates are given in (8.4).

The acoustic field will also be quantified through computations of total acoustic power. The formula for acoustic power is equation (4.4) of MK95, which can be

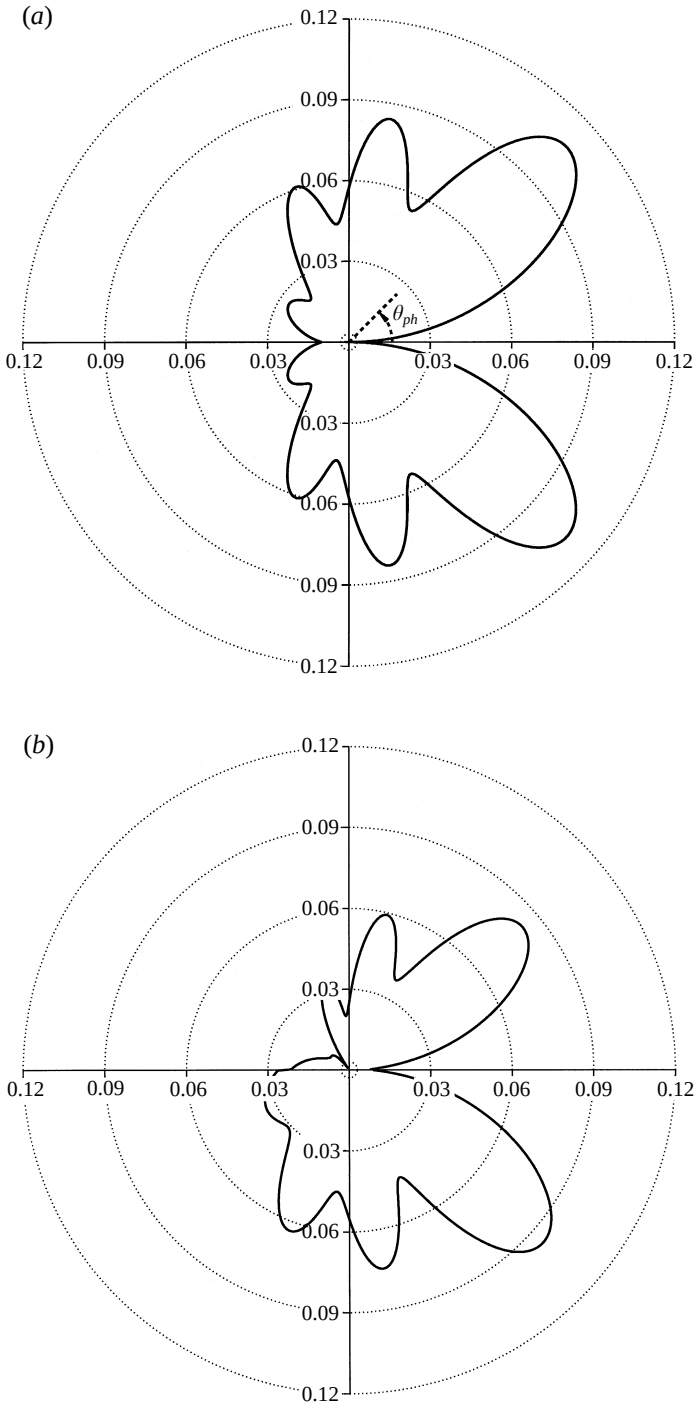

FIGURE 4(*a*, *b*). For caption see facing page.

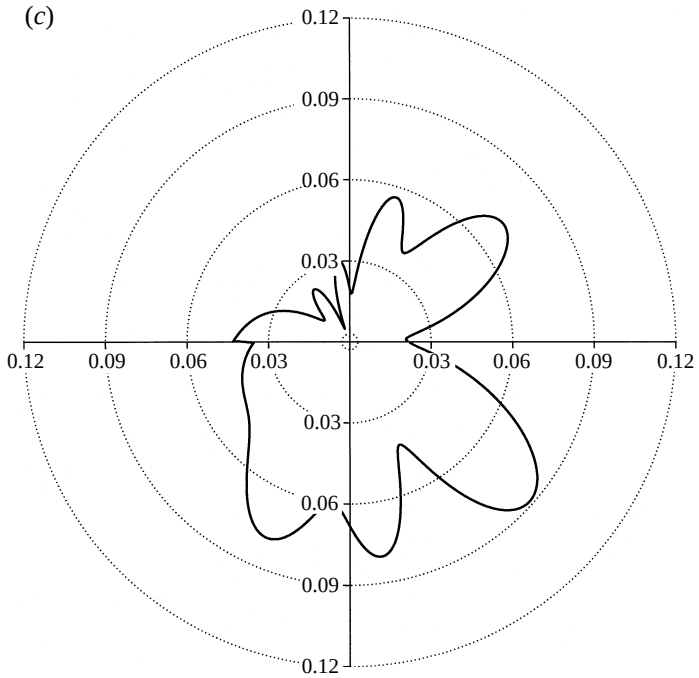

FIGURE 4. Far-field pressure directivity pattern. (*a*) Flat-plate airfoil, $\alpha_i = 0$, $M_\infty = 0.5$, $k = 8$, $\theta_g = 60°$. (*b*) 3-33 airfoil, $\alpha_i = 0$, $M_\infty = 0.5$, $k = 8$, $\theta_g = 60°$. (*c*) 6-33 airfoil, $\alpha_i = 0$, $M_\infty = 0.5$, $k = 8$, $\theta_g = 60°$.

derived from Morfey's (1971) expression for the power of a sound field in a moving medium. We repeat the formula here for convenience:

$$\text{Normalized power} = \frac{\text{Ave. power/span}}{\frac{1}{2}\rho_\infty U_\infty^3 b\epsilon^2}$$

$$= k^2 w \int_0^{2\pi} hh^*(\beta_\infty \cos^2\theta + \sin^2\theta)(\beta_\infty^2 \sin^2\theta + \cos^2\theta)^{1/2} r\mathrm{d}\theta, \quad (9.3)$$

where b is the airfoil semichord, ϵ the dimensionless gust amplitude, h is the far-field potential given in (8.2), and h^* denotes the complex conjugate.

9.2.1. *Isolated effect of camber*

The effect of airfoil camber is first examined by considering the interaction of a vortical disturbance with an airfoil having three different amounts of camber. The Mach number is 0.5, $\theta_g = 60°$, $k = 8$, and $\alpha_i = 0$. Figure 4(*a*) is a plot of the pressure directivity for zero camber. As is to be expected in the absence of mean loading, the pressure is perfectly antisymmetric and there is zero downstream radiation. In figure 4(*b*) the airfoil is the 3-33 type pictured in figure 3. Even though the maximum camber is just 3%, the pattern is quite different from that for the unloaded flat plate. Though there is still little radiation directly downstream, there is much more radiation below the airfoil than above it. When the maximum camber is raised to 6%, as for the 6-33 airfoil of figure 4(*c*), the difference between the fields above and below the airfoil is extreme. In figure 4(*c*) there is also a noticeable amount of radiation directly

downstream. The sequence of patterns in figures 4(*a*)–4(*c*) illustrates that even small amounts of airfoil camber can have a pronounced effect on the radiated sound field.

Our directivity patterns generally have a discontinuity directly upstream of the airfoil (across $\theta_{ph} = \pi$). This is a consequence of our high-frequency approximation, which consists of a primary field from the leading edge and a secondary field from the trailing edge. The primary field is discontinuous downstream of the airfoil. This discontinuity is removed by the secondary scattered field from the trailing edge, which then introduces a weaker discontinuity in the upstream direction. This upstream discontinuity would be eliminated by a tertiary scattered field from the leading edge, but the tertiary field has not been considered because it is of higher order than the terms which have been retained in our analysis.

The influence of surface curvature on acoustic propagation near the airfoil is, as noted in §9.1, accounted for in the scattered field h_{ltn}. As a special case which illustrates curved surface effects, consider flow past a curved rigid surface having the same shape as the airfoil and its mean wake. The interaction of the gust with the leading edge generates the field h_l as before, but there is no scattered field from the trailing edge (due to the presence of the rigid surface beyond $x = 2$). One then needs a transition field to account for diffraction by the curved surface. It turns out that, for the special case $\alpha_i = n'(2)$, the extension of the boundary condition for $\phi > 2$ which was utilized in (5.5*b*) is exactly that required to eliminate the transverse velocity through the wake surface. The combination $h_l + h_{ltn}$ then provides the complete solution for the acoustic field in this case.

As an example of this special case, consider the 8-32 airfoil generated by setting $a_0 = 0.288$, $a_1 = -0.60$ and $a_2 = 0.05$. This airfoil is similar in shape to the X-33, but its maximum camber occurs at 32% chord and its trailing-edge slope $n'(2)$ is zero. The acoustic field generated by interaction with a gust convected at Mach number 0.6, with $k = 8$ and $\theta_g = 45°$, is illustrated in figure 5. With α_i set to zero, the effective leading-edge incidence angle is $\alpha_{eff} = -4.13°$, producing the leading edge directivity $D_l(\theta)$ plotted as a dashed line in figure 5. Note that, even for this relatively small value of α_{eff}, the leading-edge directivity differs markedly from the $\cos\frac{1}{2}\theta$ pattern which is obtained for $\alpha_{eff} = 0$. The directivity for the combined field $h_l + h_{ltn}$ is plotted as a solid line in figure 5. The transition solution decreases the pressure field at shallow positive downstream angles, due to shadow effects associated with propagation along the convex upper surface of the airfoil. A peak in the field and a damped oscillatory pattern is seen at somewhat larger positive angles. The transition solution increases the pressure field at shallow negative downstream angles, due to whispering-gallery effects associated with propagation along the concave lower surface of the airfoil. A mild decrease in the field and a damped oscillatory pattern is seen at somewhat larger negative angles.

9.2.2. *Combined effect of camber and incidence angle*

In this subsection we explore combined effects of airfoil camber and incidence angle. We first focus on the total sound power generated by the airfoil–gust interaction. Earlier models of mean loading effects on gust interaction noise (Ffowcs Williams & Hawkings 1969*b*; Goldstein, Rosenbaum & Albers 1974; Mani 1974) utilized the Ffowcs Williams & Hawkings acoustic analogy (Ffowcs Williams & Hawkings 1969*a*), and modelled the mean flow by a row of two-dimensional point vortices superimposed on a uniform flow. Hence, the only mean-flow parameter which entered these models was the vortex strength, or equivalently the airfoil lift coefficient. We accordingly first present calculations of the sound power as a function of lift coefficient for

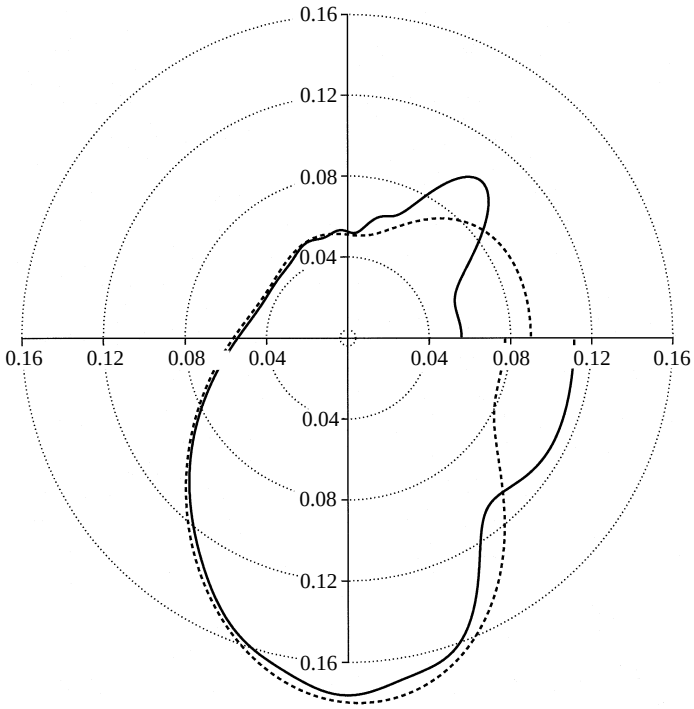

FIGURE 5. Far-field pressure directivity patterns illustrating leading-edge transition field effects. Dashed line is $D_l(\theta)$ for an 8-32 airfoil at $\alpha_i = 0$, $M_\infty = 0.6$, $k = 8$, and $\theta_g = 45°$. Solid line is $D_l(\theta) + D_{ltn}(\theta)$, for a semi-infinite surface having the same shape as the airfoil and its mean wake.

four different airfoils. The first airfoil is a flat plate at variable incidence angle. The second is an X-33 airfoil at zero incidence angle (i.e. the airfoil having the shape shown in figure 3) but with variable maximum camber. The third airfoil is a 7% camber circular arc at variable incidence angle, and the fourth is a 7-33 airfoil also at variable incidence angle. The sound power levels produced when $M_\infty = 0.6$, $k = 7$, and $\theta_g = 45°$ are plotted as a function of lift coefficient in figure 6. It is clear that the trends are highly variable: the flat plate shows a sharp increase in power with total loading, the 7-33 airfoil a sharp decrease, and the circular arc and X-33 airfoil little change.

Since our high-frequency theory shows that the sound generation is concentrated in the local leading-edge region, where α_{eff} is the relevant mean-loading parameter, we investigated the utility of replotting the sound power data of figure 6 against $\alpha_{eff}/\beta_\infty$. The result is shown in figure 7(*a*). The curves are nearly indistinguishable, demonstrating that α_{eff} is an extremely useful correlating parameter for mean-loading effects, at least under the parametric conditions leading to figures 6 and 7(*a*).

In figure 6, the very different results for the different airfoils can be understood in terms of the relationship between α_{eff} and the lift coefficient. For the flat plate $C_L/2\pi$ is equal to $\alpha_{eff}/\beta_\infty$, and the rapid increase in power with lift coefficient matches the rapid increase in power with positive $\alpha_{eff}/\beta_\infty$. For the circular arc and 7-33 airfoils, a negative incidence angle is required in order to achieve a zero or slightly positive lift coefficient. When the negative incidence angle is combined with the value $\alpha_{1_c} = 0$ for the circular arc and $\alpha_{1_c} = 0.051$ for the 7-33 airfoil, α_{eff} is slightly negative for the circular arc and more negative for the 7-33 airfoil. From figure 7(*a*), then, one can

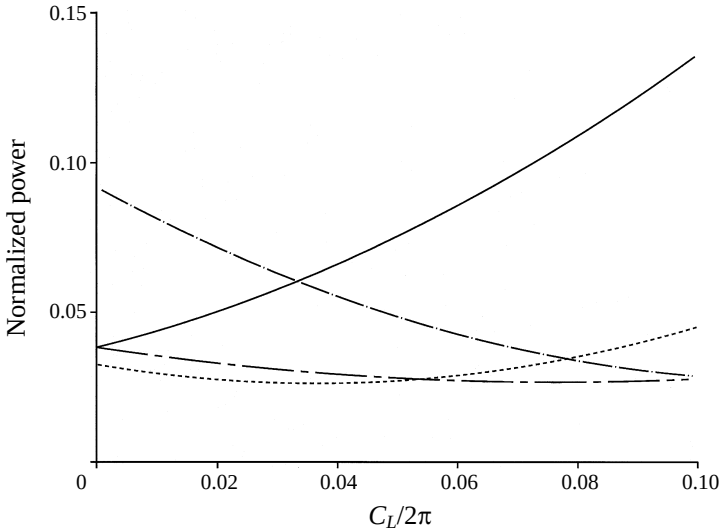

FIGURE 6. Radiated acoustic power versus lift coefficent for four airfoils: a flat plate at variable incidence angle (solid line), variable-camber X-33 airfoil at zero incidence angle (small and large dashes), 7% camber circular arc at variable incidence angle (small dashes), and 7-33 airfoil at variable incidence angle (dashes and dots). $M_\infty = 0.6$, $k = 7$, $\theta_g = 45°$.

see that in figure 6 the circular arc airfoil is in a range where the power is relatively insensitive to changes in α_{eff} and the 7-33 airfoil is in a range (off the graph to the left) where the power decreases relatively rapidly as α_{eff} increases. Finally, for the X-33 airfoil at zero incidence angle, increasing the lift coefficient by raising the camber moved α_{eff} from zero to negative values, in a range where the power is insensitive to changes in α_{eff}. Thus in figure 6 the power for the X-33 airfoil varied only slightly with lift coefficient.

To evaluate the degree of correlation of the acoustic power with α_{eff} for other parameter values, we performed similar computations at a reduced frequency $k = 2$, with the Mach number and gust angle remaining at 0.6 and 45°, respectively. Since variations between power curves plotted against α_{eff} are primarily due to trailing-edge effects (the transition regions affecting the intensity only at shallow angles), one might expect a poorer correlation at lower reduced frequencies, where the trailing-edge radiation is stronger. Although the collapse of the results in figure 7(b) is not quite as good as in figure 7(a), the degree of correlation provided by the parameter α_{eff} is surprisingly high, when one considers that the large parameter k is only 2.

The high degree of correlation holds for a gust orientation angle of $\theta_g = 0$ as well, as is evident in figure 7(c). The near symmetry across $\alpha_{eff} = 0$ exhibited in figure 7(c) is sensible on physical grounds: for $\theta_g = 0$ the gust velocity oscillates vertically, and a flat plate at an incidence angle α should produce the same power as a flat plate at incidence angle $-\alpha$. Likewise, when the velocity fluctuations are vertical a 'concave-down' airfoil should generate the same power as the corresponding 'concave-up' airfoil. Symmetry across $\alpha_{eff} = 0$ cannot be expected when incidence angle and camber are combined, since the combination of incidence angle and camber can be manipulated to alternately yield the values α_{eff} and $-\alpha_{eff}$ without symmetrically inverting the geometry. Nevertheless, a high degree of symmetry exists in figure 7(c) for the combined incidence angle and camber cases.

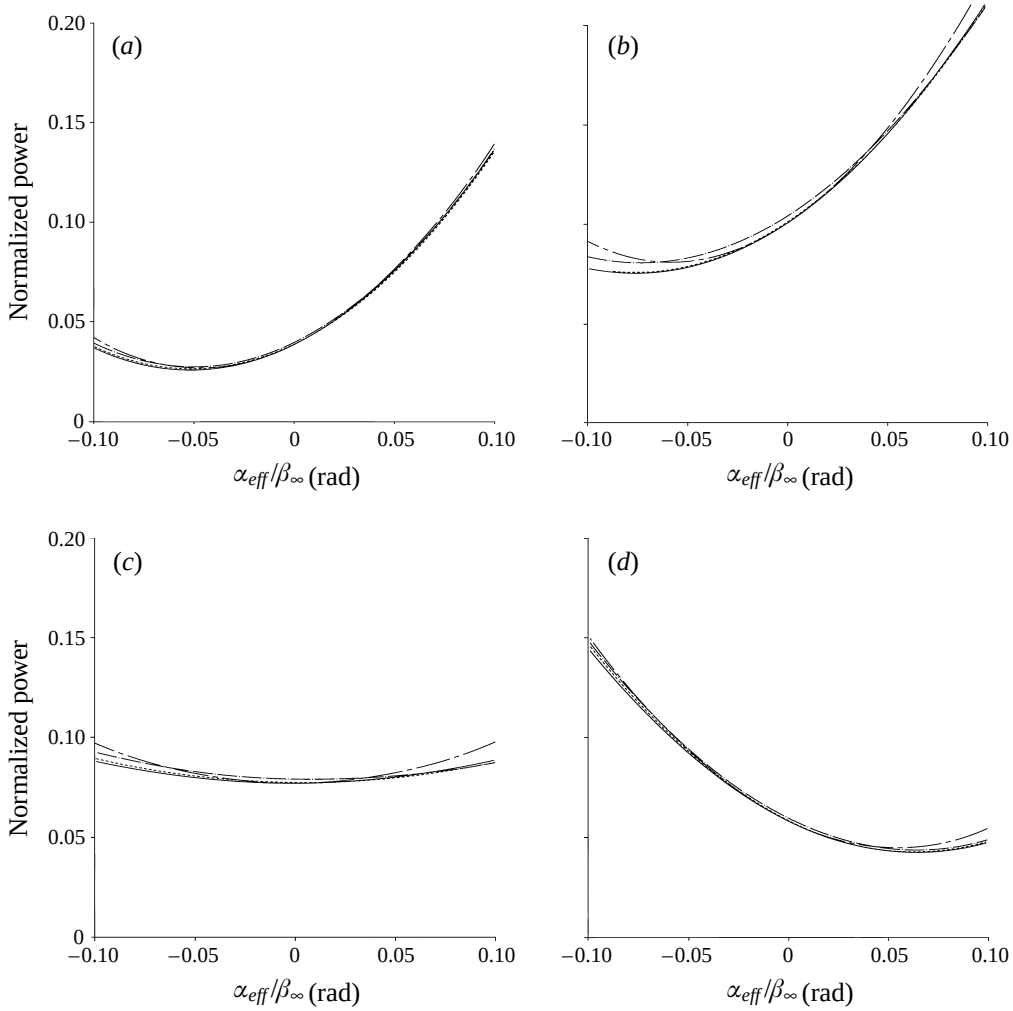

FIGURE 7. Radiated acoustic power versus $\alpha_{eff}/\beta_\infty$ for the four airfoils of figure 6. $M_\infty = 0.6$. (*a*) $k = 7$, $\theta_g = 45°$; (*b*) $k = 2$, $\theta_g = 45°$; (*c*) $k = 7$, $\theta_g = 0$; (*d*) $k = 7$, $\theta_g = -30°$.

Normalized power calculated for a final gust angle, $\theta_g = -30°$, is plotted in figure 7(*d*). Once again the correlation is seen to be very good. In contrast to the curves for positive values of θ_g, for negative θ_g the power decreases with increasing α_{eff} over most of the α_{eff} values of interest. In fact, by the symmetry arguments discussed in the previous paragraph, the curves for negative values of θ_g can be shown to be near mirror images across $\alpha_{eff} = 0$ of the curves existing for positive θ_g. A practical implication of figure 7(*a–d*) is that the sound power can increase, decrease, or remain effectively unchanged with increased leading edge incidence angle α_{eff}. It is therefore important that detailed characteristics of the gust spectrum be considered when assessing the influence of mean loading. It is interesting to note that fan–viscous-wake interactions typically involve positive gust angles, often on the order of 45°.

While α_{eff} is essentially the only important mean-loading parameter for predicting the integrated quantity of total acoustic power, the same is not true for determining local quantities such as acoustic pressure. We now consider three cases for which

α_{eff} is zero and the normalized power is approximately 0.014. The Mach number is 0.5, the reduced frequency 8.0, and the gust angle 60°. The airfoil in the first case is simply a flat plate, and the pressure directivity pattern is given in figure 4(*a*). As noted previously, this pattern exhibits antisymmetry across the airfoil and no downstream radiation. The second case, shown in figure 8(*a*), is a 6-33 airfoil at an angle of attack of 2.5°. The directivity pattern of figure 8(*a*) begins to exhibit asymmetry from top to bottom and some radiation in the downstream direction. The downstream radiation arises because the $O(\alpha_g k)$ phase shifts have begun to produce a non-zero average pressure across the trailing edge, which continues in the downstream direction. The asymmetry and downstream radiation are accentuated when the incidence angle is increased to 5° and the maximum camber to 12%, as shown in figure 8(*b*). The angle of maximum radiation in the upper half-plane for figure 4(*a*) resides near a local minimum in figure 8(*b*). The total number of lobes is the same in each of the patterns in 4(*a*), 8(*a*), and 8(*b*), but the number of lobes in the upper half-plane relative to that in the lower increases with increasing loading.

In figure 9, the directivity pattern is presented for the same case as in figure 8(*b*), except that the Mach number has been raised from 0.5 to 0.75. The increase in Mach number has led to a number of significant changes in the directivity pattern. First, the phase distortion of the leading-edge ray field due to mean-loading effects has increased (see (9.1)), so that the rays impinging on the upper and lower surfaces of the trailing edge have been shifted nearly into phase, weakening the scattered field from the trailing edge. Thus, the modulation of the directivity pattern is smaller in amplitude than in figure 8(*b*). In fact, for the conditions of figure 9 the scattering of the leading-edge transition field h_{ltn} by the trailing edge is nearly as important as the scattering of the leading-edge ray field h_l. The sum of the leading-edge transition field and its scattered field by the trailing edge is plotted as a dashed line in figure 9. This sum has two strong lobes, one about 25° above the wake and one 25° below it. The top lobe adds out of phase with the $\cos\frac{1}{2}\theta$ leading-edge ray pattern and the bottom lobe adds in phase, producing a noticeable local minimum and maximum, respectively, in the overall pattern.

It is interesting to note that the modulation of the directivity pattern in figure 9 is more rapid in the upper half-plane than in the lower, and that in both half-planes the modulation becomes much more rapid as the upstream direction is approached. These features can be explained by examining the influence of the mean loading on the relative phases of the leading-edge and trailing-edge ray fields. In the far field, the difference in phase is given by

$$\sigma_l - \sigma_t = 2w\cos\theta + 2\frac{\alpha_i}{\beta_\infty}V(\theta)\sin\theta \pm \pi\frac{\alpha_g}{\beta_\infty}(V(\theta)+w)\cos\theta, \tag{9.4}$$

where the $\pm$ sign applies in the upper and lower half-planes, respectively, and $V(\theta)$ is defined in (4.1*d*). It is the variation of the relative phase with angle, coupled with any angular variations in the phases of the leading- and trailing-edge directivity functions, that produces the modulation in the far-field pattern.

Only the first term of (9.4) is present when there is no mean loading; this term arises due to differences in the distance to a far-field point, and is responsible for the modulation seen in figure 4(*a*). For the conditions of figures 8 and 9, the third term of (9.4), which is proportional to the total-loading parameter α_g, is the dominant mean-loading effect. This term adds to the variation of the relative phase in the upper half-plane, producing a more rapid modulation, while in the lower half-plane the first and third terms act in opposition, decreasing the rate of modulation of the far-field

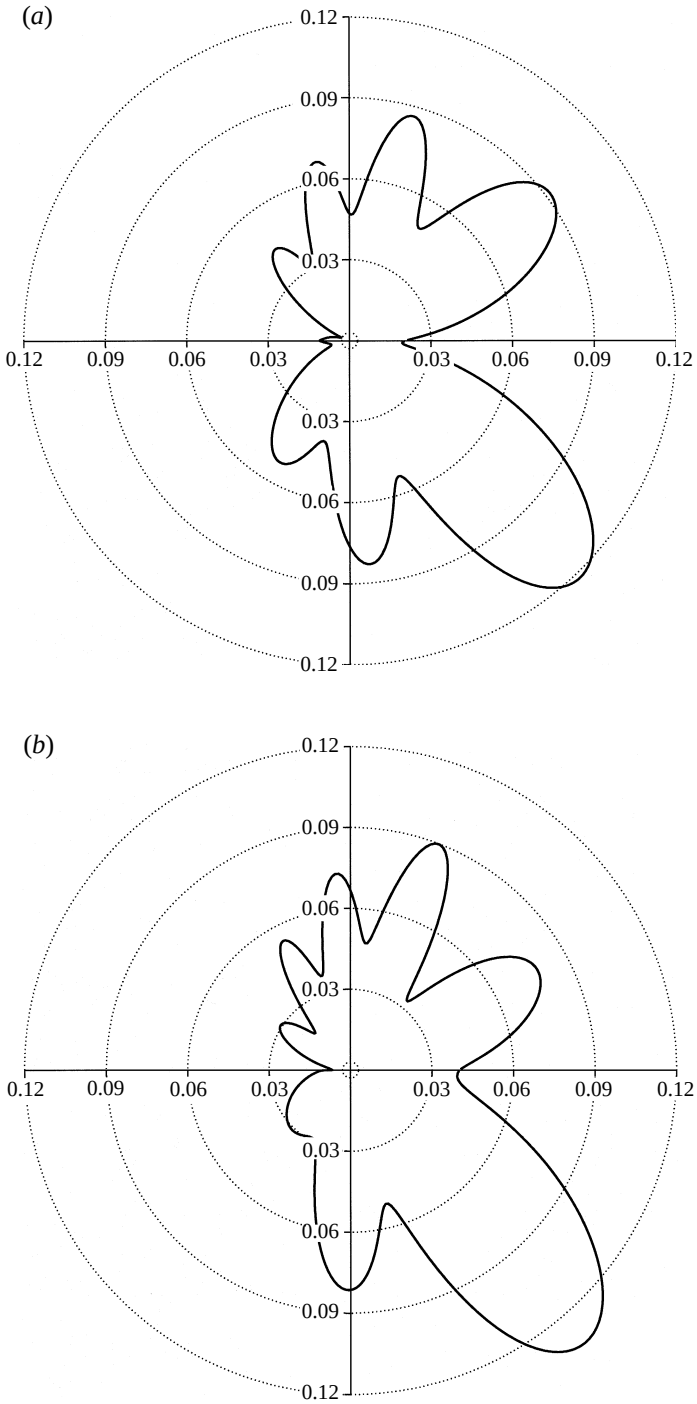

FIGURE 8. Far-field pressure directivity pattern for (*a*) a 6-33 airfoil at an incidence angle of 2.5°, (*b*) a 12-33 airfoil at an incidence angle of 5°. $M_\infty = 0.5$, $k = 8$, $\theta_g = 60°$.

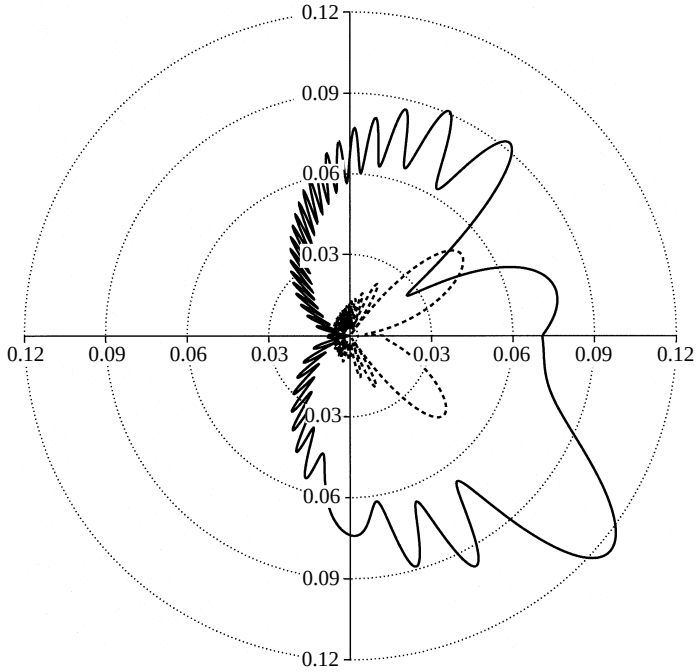

FIGURE 9. Far-field pressure directivity patterns for a 12-33 airfoil at an incidence angle of 5°. $M_\infty = 0.75$, $k = 8$, $\theta_g = 60°$ Total field is denoted by solid line; leading-edge transition field plus its scattered field denoted by dashed line.

pattern. Physically, the perturbation flow speed q associated with the mean loading is positive above the airfoil, resulting in a larger convection speed which an acoustic wave travelling upstream from the trailing edge must oppose in order to interfere with the wave from the leading edge. In contrast, q is negative below the airfoil, decreasing the convection speed and thus reducing the modulation of the directivity pattern.

The increased modulation in the upper half-plane relative to that in the lower is a mean-loading effect that also occurs at modest Mach numbers, as can be seen from figure 8. In contrast, the very rapid modulation in the upstream direction is a mean-loading effect that becomes important only at high subsonic Mach numbers. This effect is caused by the second term of $V(\theta)$, which (for $k_3 = 0$) is proportional to $M_\infty^3 \beta_\infty^{-4}(1 - M_\infty \cos\theta)^2$. Thus, at high subsonic Mach numbers, $V(\theta)$ takes on large values in the upstream direction, causing the rapid modulation of the upstream field seen in figure 9. Physically, this strong influence of mean loading on the upstream modulation arises because acoustic waves propagating upstream in a nearly sonic flow travel quite slowly, increasing the time over which the mean-flow perturbation can act to modify the phase of the waves.

9.2.3. *Dependence of the sound field upon gust characteristics*

In this subsection we consider the dependence of the sound field on gust characteristics. Even with the restriction to two-dimensional gusts, it is impractical to fully explore the behaviour of the pressure directivity fields throughout the parameter space of Mach number, frequency, airfoil, and gust characteristics. In the previous subsection, we found that the influence of camber and incidence angle on the total

acoustic power is well correlated by the effective leading-edge incidence angle, α_{eff}. This is also the only mean-loading parameter which enters the directivity pattern of the leading-edge ray field. Since the trailing-edge and transition fields serve only to modify the basic directivity pattern of the leading-edge field, in this subsection we examine the influence of gust characteristics on the leading-edge ray field.

In examining the leading-edge ray field in isolation, it is advantageous to introduce a modified acoustic power and pressure which absorb some of the dependence on frequency and Mach number. We define

$$\text{Leading-edge power} = \text{Normalized power}\left(\frac{k}{M_\infty}\right). \tag{9.5}$$

The analogous leading-edge pressure is defined as $k^{1/2}|p|r_{ph}^{1/2}$. When α_{eff} is zero, the leading-edge sound field is a pole of $\frac{3}{2}$-order with pressure directivity $\cos\frac{1}{2}\theta$, intermediate between a monopole and dipole. The acoustic power for a two-dimensional pole of $\frac{3}{2}$-order scales as M_∞^4, and is inversely proportional to frequency, so that the leading edge power and pressure for $\alpha_{eff} = 0$ depend only on the gust angle θ_g. For non-zero values of α_{eff}, leading-edge power and pressure are a function of $\alpha_{eff}k^{1/2}$ and θ_g in the low-Mach-number limit, while additional dependence on M_∞ is present at $O(1)$ Mach numbers. Results will be presented for positive values of α_{eff}. The corresponding results for negative values of α_{eff} can be obtained by reversing the sign of θ_g.

In figure 10, the leading-edge power generated by interaction with a vorticity gust is plotted as a function of gust angle, for values of the mean loading parameter $\alpha_{eff}k^{1/2}$ equal to 0, 0.1, 0.2, and 0.3. The Mach number is 0.6. For zero α_{eff}, noise is generated only by the airfoil surface blocking the normal component of gust velocity, and the power curve has the simple $\cos^2\theta_g$ dependence ($\cos\theta_g$ being the normal velocity component for the vorticity gust). Modest amounts of mean loading increase the sound power for positive gust angles and decrease it for negative θ_g. As the mean loading is increased, the maximum of the curve rises rapidly and its location shifts to positive values of θ_g.

The leading-edge pressure directivities for the case of $M_\infty = 0.6$, $\theta_g = 45°$, and varying amounts of mean loading are shown in figure 11. The increase in pressure magnitude as the loading parameter is raised from 0 to 0.3 reflects the increase in power seen in figure 10. While no radical change in shape is observed with increasing mean loading, a significant increase in the amount of upstream radiation can be observed. Leading-edge directivities were also generated for gust orientation angles of $-30°$, 0, and $30°$, for $M_\infty = 0.6$ and $\alpha_{eff}k^{1/2} = 0.2$. The plots (figure 12) show that the amount of radiation above the airfoil relative to the amount below increases substantially as the orientation angle is decreased.

Figure 13(*a*) illustrates the influence of Mach number on the generated sound power. The leading-edge power is plotted as a function of gust angle, with $\alpha_{eff}k^{1/2} = 0.2$, for four Mach numbers in the range 0 to 0.75. The curves for $M_\infty = 0$ and 0.25 verify the independence of leading-edge power upon Mach number for small M_∞. As the Mach number increases beyond 0.5, the leading-edge power rapidly increases. The gust angle of maximum power stays relatively constant, however, at around $30°$.

The dependence upon compressibility illustrated in figure 13(*a*) can be further correlated, in the following way. It is well known that airfoil steady loading increases with Mach number, and that within the framework of thin-airfoil theory compressibility effects can be accounted for by the introduction of a Prandtl–Glauert factor

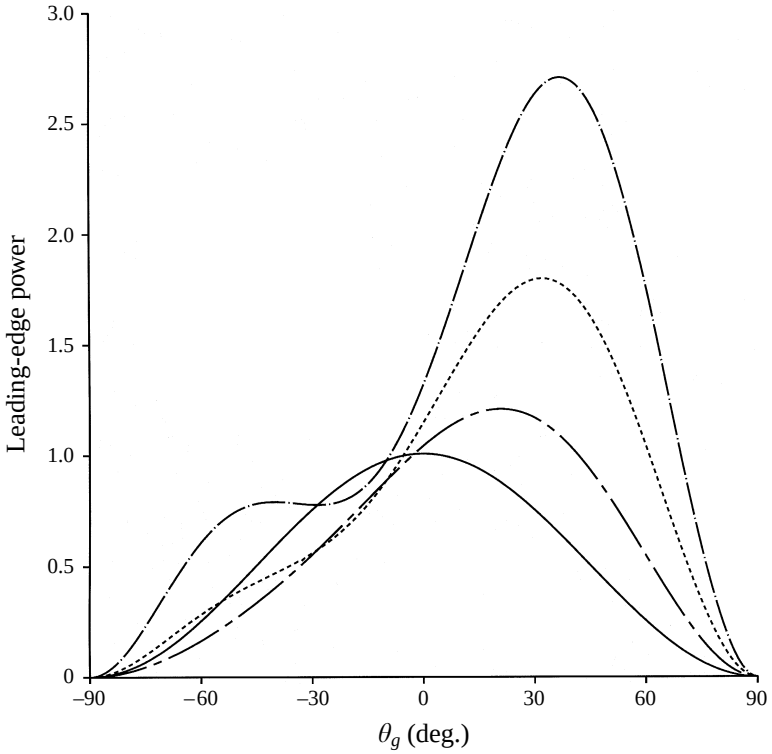

FIGURE 10. Leading-edge power versus gust orientation angle, for $\alpha_{eff}k^{1/2} = 0$ (solid line), 0.1 (small and large dashes), 0.2 (small dashes), and 0.3 (dashes and dots). $M_\infty = 0.6$.

$1/\beta_\infty$ into the lift coefficient. To determine if a similar approach would capture at least the major influences of compressibility on unsteady airfoil–gust interactions, we considered the modified leading-edge loading parameter $\alpha_{eff}k^{1/2}/\beta_\infty$. In figure 13($b$), the leading-edge power is plotted for the same four Mach numbers as in figure 13(a), but with the leading-edge loading held constant through the parameter $\alpha_{eff}k^{1/2}/\beta_\infty$ rather than $\alpha_{eff}k^{1/2}$. It can be seen that the inclusion of the Prandtl–Glauert factor has significantly reduced the variations between the different curves.

We next consider the influence of mean loading on the sound power generated by entropy gusts. Far upstream, a purely entropic gust has density fluctuations, but no velocity or pressure fluctuations. The entropy gust generates sound only by its interaction with the mean-flow gradients. Since the gust modifies the density of the fluid particle, in passing through the mean pressure gradient an under-acceleration or over-acceleration of the fluid particle occurs, resulting in velocity fluctuations. These velocity fluctuations then generate sound in two ways: through unsteady interactions with rigid surfaces, and through gradients of the Reynolds stress components which contain products of the mean and fluctuating velocities.

In figure 13(c) we plot the leading-edge power produced by the interaction of a purely entropic gust ($\boldsymbol{A} = \boldsymbol{0}$, $B = 1$ in (2.1)) with an airfoil having three different values of mean loading. The Mach number is 0.6. For all values of $\alpha_{eff}k^{1/2}$, the power is maximum at $\theta_g = 0$, and the curves are symmmetric about this angle of maximum power. The amount of acoustic power is seen to be low for small values of α_{eff}; in fact, it can be shown that the acoustic power for a purely entropic gust is $O(\alpha_{eff}^2)$

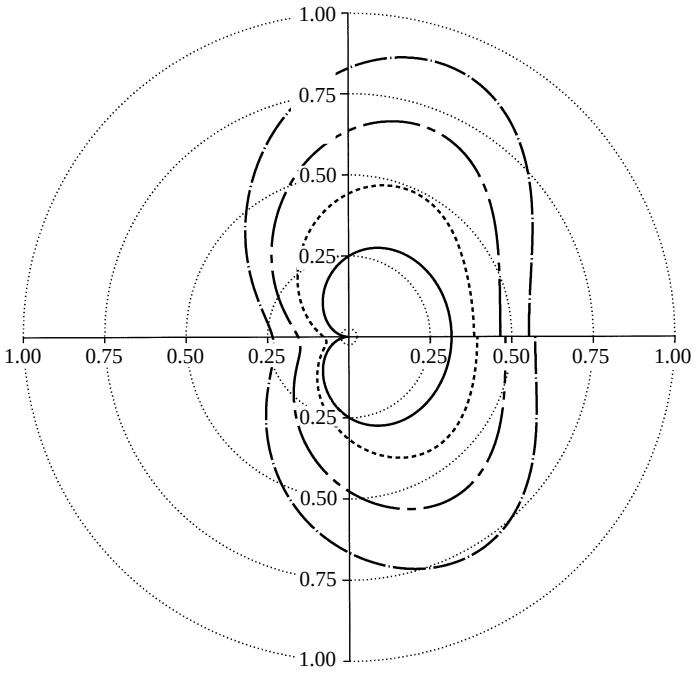

FIGURE 11. Far-field directivity pattern for leading-edge pressure. $M_\infty = 0.6$, $\theta_g = 45°$. $\alpha_{eff}\, k^{1/2} = 0$ (solid line), 0.1 (small dashes), 0.2 (small and large dashes), and 0.3 (dashes and dots).

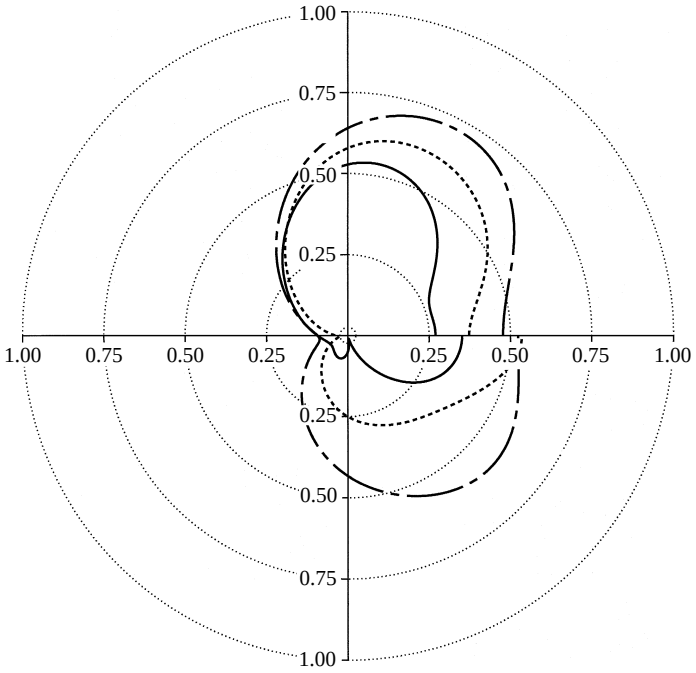

FIGURE 12. Far-field directivity pattern for leading-edge pressure. $M_\infty = 0.6$, $\alpha_{eff}\, k^{1/2} = 0.2$, $\theta_g = -30°$ (solid line), 0° (small dashes), and 30° (small and large dashes).

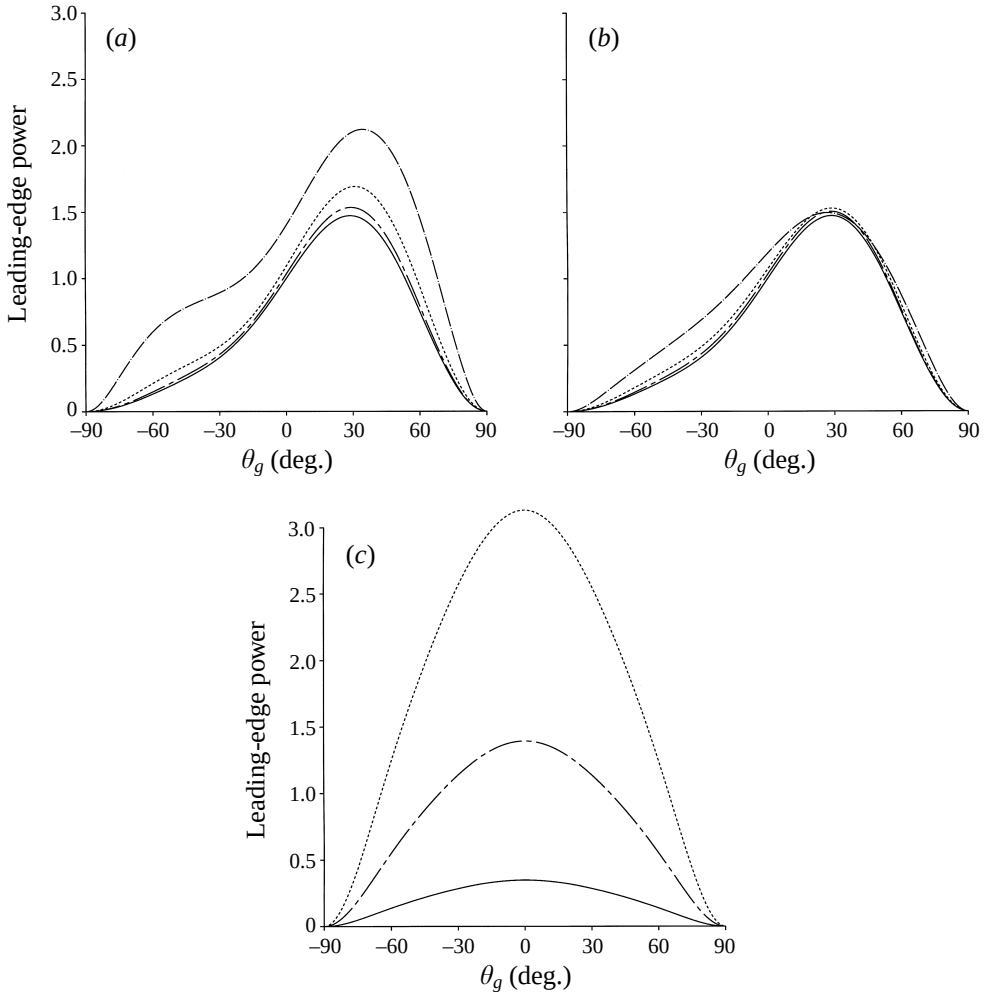

FIGURE 13. Leading-edge power versus gust orientation angle, for (*a*) Mach numbers of 0 (solid line), 0.25 (small and large dashes), 0.5 (small dashes), and 0.25 (dashes and dots). $\alpha_{eff} k^{1/2} = 0.2$, (*b*) same as in (*a*) but with $\alpha_{eff} k^{1/2}/\beta_\infty = 0.2$, (*c*) a purely entropic gust, with $\alpha_{eff} k^{1/2} = 0.1$ (solid line), 0.2 (small and large dashes), and 0.3 (small dashes). $M_\infty = 0.6$.

as $\alpha_{eff} \to 0$. For a purely entropic gust, the $O(\alpha_{eff} k^{1/2})$ fluctuating Reynolds stress (contained in H_2) is the only sound-generating mechanism which enters our analysis; the interaction of the velocity fluctuation with the leading edge is only $O(\alpha_{eff})$ (see (2.6)) and therefore too small to be retained in our approximation. No sound is generated by an entropy gust interacting with an unloaded leading edge. In contrast, velocity fluctuations are present for a vortical gust even in the absence of mean-flow acceleration, and the blocking of these fluctuations by the airfoil surface generates a sound field even when $\alpha_{eff} = 0$ (figure 10).

Leading-edge pressure directivities for the case of an entropy gust and a Mach number of 0.6 are plotted in figure 14. When the gust orientation angle is $\theta_g = 0$, nearly all of the radiation is downstream. A progressive shift toward increasing upstream radiation is seen as the orientation angle is raised to 30° and 60°. The mean-loading parameter in figure 14 is $\alpha_{eff} k^{1/2} = 0.2$, but since the leading-edge

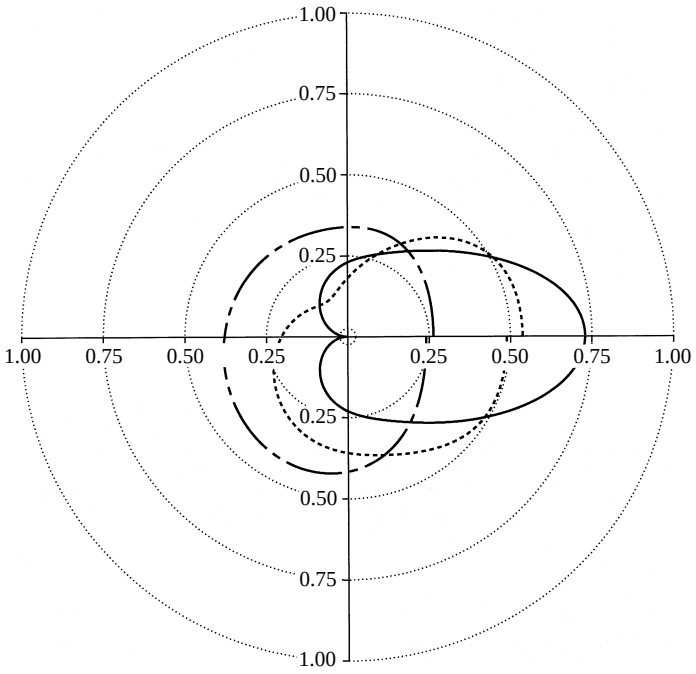

FIGURE 14. Far-field directivity pattern for leading-edge pressure. Entropy gust, with $M_\infty = 0.6$, $\alpha_{eff}\, k^{1/2} = 0.2$, $\theta_g = 0°$ (solid line), 30° (small dashes), and 60° (small and large dashes).

pressure is proportional to $\alpha_{eff} k^{1/2}$ for a purely entropic gust, the directivity shape is identical for all values of $\alpha_{eff} k^{1/2}$ (satisfying $\alpha_{eff} k^{1/2} \ll 1$). Also, the leading-edge pressure directivity patterns for negative gust angles are the mirror images (across $x_2 = 0$) of those for positive θ_g.

To observe the effect of Mach number on the sound generated by entropy gusts, results for $M_\infty = 0.0, 0.25, 0.5$, and 0.75 are presented in figure 15(*a*). The leading-edge loading is $\alpha_{eff} k^{1/2} = 0.2$. The power is seen to increase significantly with increasing Mach number, even more than for a vorticity gust (figure 13(*a*)). To determine whether the increase in leading-edge power with Mach number could be captured by the Prandtl–Glauert factor $1/\beta_\infty$ amplifying the mean lift coefficient, we computed the acoustic power for the same four Mach numbers of figure 15(*a*), but with the modified loading parameter $\alpha_{eff} k^{1/2}/\beta_\infty$ held constant at 0.2. The results (figure 15(*b*)) show that, as with vorticity gusts, inserting the factor $1/\beta_\infty$ into the mean loading parameter provides a reasonable collapse of compressibility effects.

For relatively high subsonic Mach numbers, the pressure directivities for both the isolated vorticity and entropy gusts begin to show noticeable lobing. In figure 16 the directivities are plotted for the case $M_\infty = 0.75, \theta_g = 0$, and $\alpha_{eff} k^{1/2} = 0.2$. The lobing is due in part to the interactions between the components of the fluctuating Reynolds stress, some of which become important at high Mach numbers due to their β_∞^{-6} dependence (MK95). The emerging acoustic-propagation effects, which are proportional to β_∞^{-8} (MK95), contribute to further lobing for the vorticity gust. It is interesting to note that, while the vorticity and entropy gusts of figure 16 radiate almost the same maximum pressure, these maxima occur in nearly orthogonal directions.

A comparison of sound-power levels for isolated vorticity and entropy gusts, especially those plotted in figures 13(*b*) and 15(*b*), shows that the maximum power

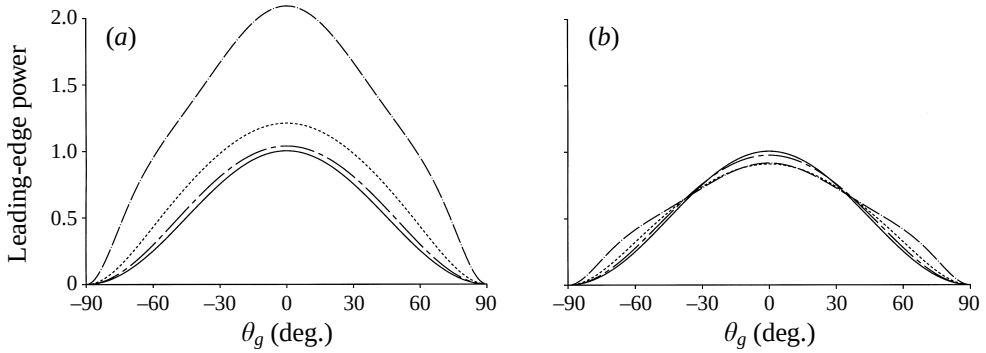

FIGURE 15. Leading-edge power versus gust orientation angle for a purely entropic gust, with $M_\infty = 0$ (solid line), 0.25 (small and large dashes), and 0.5 (small dashes), and 0.75 (dashes and dots). (*a*) $\alpha_{eff} k^{1/2} = 0.2$, (*b*) $\alpha_{eff} k^{1/2}/\beta_\infty = 0.2$.

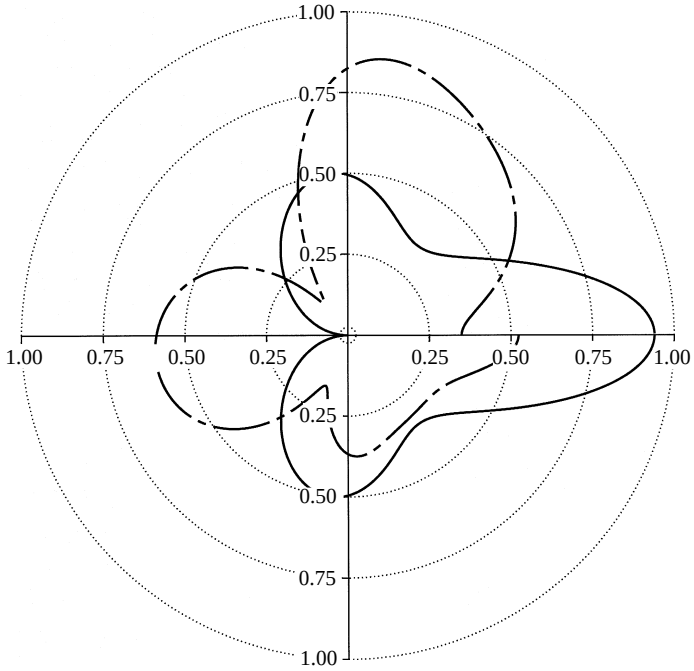

FIGURE 16. Far-field directivity pattern for leading-edge pressure, for a purely entropic gust (solid line) and a purely vortical gust (small and large dashes). $M_\infty = 0.75$, $\alpha_{eff} k^{1/2} = 0.2$, $\theta_g = 0$.

levels for vorticity gusts generally exceed those for entropy gusts when $\alpha_{eff} k^{1/2}/\beta_\infty$ is less than 0.3, while the maximum power levels for entropy gusts are larger when $\alpha_{eff} k^{1/2}/\beta_\infty$ exceeds 0.3. We next briefly consider the case where vorticity and entropy gusts are present simultaneously. In general, the harmonic vorticity and entropy disturbances in (2.1) will not be in phase, so we allow the entropy amplitude to be complex in order to accomodate a phase shift.

Our first illustration of combined-gust effects considers five gusts with the following characteristics: (*i*) purely entropic, (*ii*) entropy amplitude twice the vorticity amplitude, (*iii*) vorticity and entropy amplitudes equal, (*iv*) vorticity amplitude twice the entropy

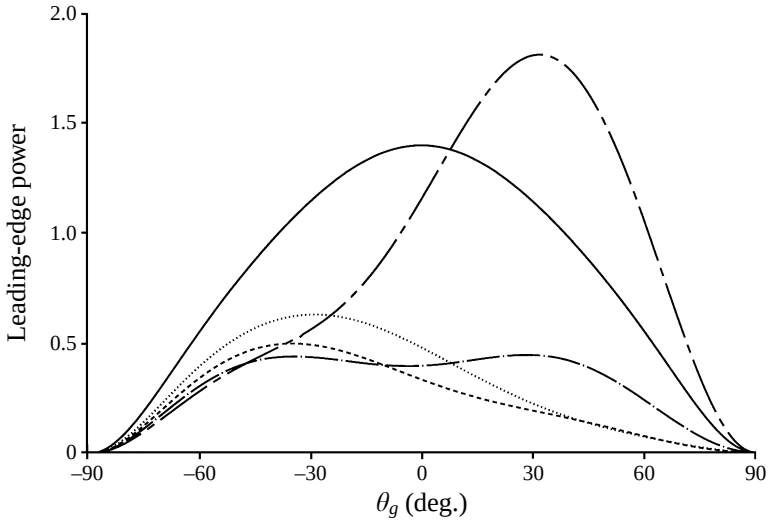

FIGURE 17. Leading-edge power versus gust orientation angle for vorticity and entropy gusts, combined in phase. Relative amplitude combinations are: $|\mathbf{A}| = 0$, $B = 1$ (solid line); $|\mathbf{A}| = 0.33$, $B = 0.67$ (dotted line); $|\mathbf{A}| = 0.5$, $B = 0.5$ (dashed line); $|\mathbf{A}| = 0.67$, $B = 0.33$ (dashed-dotted line); and $|\mathbf{A}| = 1$, $B = 0$ (small and large dashes). $\alpha_{eff}\, k^{1/2} = 0.2$, $M_\infty = 0.6$.

amplitude, and (v) purely vortical. The leading-edge power for these five gusts is plotted in figure 17, for the case $\mathrm{Arg}(B) = 0$, $M_\infty = 0.6$, and $\alpha_{eff} k^{1/2} = 0.2$. As expected the maximum power level for the purely vortical gust exceeds that for the purely entropic gust, but it is interesting that the maximum sound power levels for the combined gusts are well below the maximum levels for either type of gust in isolation. We find quite generally that, when the vorticity and entropy disturbances are combined in phase, the power for a combined gust is less than the maximum of the power levels for the isolated gust. For $\alpha_{eff} k^{1/2}/\beta_\infty < 0.3$, this maximum corresponds to the isolated vorticity gust.

We next consider vorticity and entropy gusts combined with equal amplitudes but 0°, 45°, 90°, 135°, and 180° out of phase. The leading edge power for these five gusts is plotted in figure 18, for the case $M_\infty = 0.6$ and $\alpha_{eff} k^{1/2} = 0.2$. Starting from the case $\mathrm{Arg}(B) = 0$ (corresponding to figure 17), the acoustic power is seen to rise rapidly with increasing phase difference until the gusts are about 90° out of phase. The gust orientation angle of maximum power also increases monotonically as $\mathrm{Arg}(B)$ is varied from 0 to 90°, starting from about $\theta_g = -40°$ and converging to a value around +30°. (Interestingly, a similar migration of the maximum of the acoustic power curve toward $\theta_g = 30°$ occurs in figure 10, where the gust is purely vortical and the amount of steady loading is the varied parameter.) As the phase difference $\mathrm{Arg}(B)$ increases from 90° to 180°, the power changes only slightly. For values of $\mathrm{Arg}(B)$ beyond 180°, the leading-edge power curves display a near monotonic decrease in maximum power with increasing $\mathrm{Arg}(B)$, until the power curve for $\mathrm{Arg}(B) = 0$ is recovered at $\mathrm{Arg}(B) = 360°$. We note that the maximum power levels for several of the out-of-phase combined gusts in figure 18 are comparable to the largest levels in figure 17, which correspond to the isolated vorticity and entropy gusts. Thus, while further computations remain to be done to fully characterize combined-gust effects, we conclude that relative phase has a strong influence on the level of the radiated acoustic power.

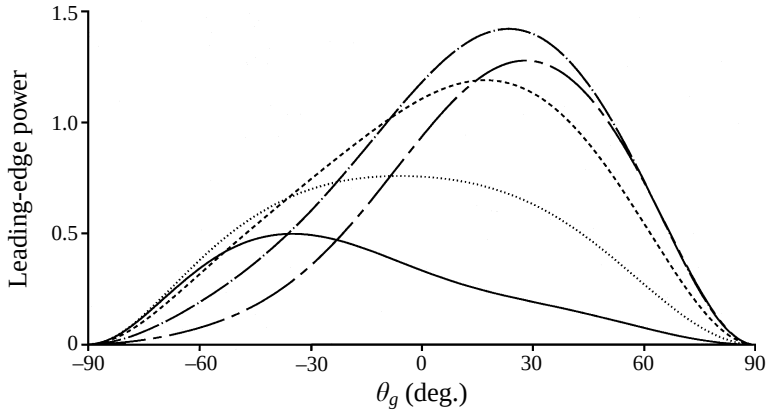

FIGURE 18. Leading-edge power versus gust orientation angle for combined vorticity and entropy gusts combined in equal amplitudes ($|\boldsymbol{A}| = 0.5$, $B = 0.5$) but with a phase difference given by $\mathrm{Arg}\,(B) = 0°$ (solid line), 45° (dots), 90° (small dashes), 135° (dashes and dots), and 180° (small and large dashes). $\alpha_{eff}\, k^{1/2} = 0.2$, $M_\infty = 0.6$.

10. Conclusion

The present work has considered the combined effects of airfoil camber and incidence angle on the sound field generated by interaction with high frequency gusts. Two important parameters arise naturally in the analysis. These are the effective leading-edge incidence angle, α_{eff}, and the toal loading parameter, α_g. These parameters are given by expressions which contain both the airfoil incidence angle and its camber distribution.

The parameter α_{eff} is a measure of the strength of the component of mean flow around the leading edge, from the lower surface to the upper. Physically, this local mean-flow component for the cambered airfoil is identical to that for a flat-plate airfoil at angle α_{eff}. For high frequency gusts ($k \gg 1$), the primary noise sources are located in the local leading-edge region – a region surrounding the leading edge which scales on the gust wavelength. The relative strength of the steady-loading related noise sources in the local leading-edge region is proportional to $\alpha_{eff}\, k^{1/2}$.

The sound field generated in the local leading-edge region propagates away to the far field according to ray theory. Two rays propagate along the airfoil upper and lower surfaces, respectively, and are scattered at the trailing edge. The strength of the scattered field from the trailing edge is proportional to the pressure jump of the leading-edge field across the trailing edge, and here the total-loading parameter α_g enters in the solution. Physically, the steady lift force for the cambered airfoil is identical to that for a flat-plate airfoil at incidence angle α_g. The acoustic rays which propagate along the upper and lower surfaces of the airfoil experience phase distortions due to the airfoil steady loading; these phase distortions are proportional to $\alpha_g k$ and are of equal magnitude but opposite sign on the two sides of the airfoil. Often, the phase distortions due to steady loading cause a significant decrease in the amplitude of the scattered field from the trailing edge. The acoustic boundary layers on the surfaces of the cambered airfoil introduce a weaker $O(\alpha k^{1/2})$ contribution to the amplitude of the scattered field from the trailing edge.

The far-field sound is a combination of the primary ray field from the leading edge and the secondary ray field from the trailing edge. Additional transition-region effects are present at shallow angles downstream of the airfoil. Constructive and destructive

interference between the leading-edge field and trailing-edge field occurs alternately as the observation angle is varied. Due to this alternation, the secondary field from the trailing edge has little impact on the toal sound power radiated to the far field, although it affects the directivity. Thus, the influence of airfoil steady loading on the total sound power is correlated very well by the aerodynamic parameter α_{eff}.

Since the trailing-edge and transition fields introduce only secondary modulations of the primary field from the leading edge, we have investigated the toal sound power levels and directivity patterns associated with the leading-edge ray field, as a function of gust characteristics and Mach number. For vortical gusts with even small amounts of loading ($\alpha_{eff} k^{1/2} > 0.1$), the maximum sound power occurs for a gust orientation angle θ_g in the vicinity of 30°, while for entropy gusts the maximum sound power occurs for $\theta_g = 0$. The single parameter $\alpha_{eff} k^{1/2}/\beta_\infty$ provides a useful quantity for correlating results generated at different amounts of steady loading and compressibility. For $\alpha_{eff} k^{1/2}/\beta_\infty < 0.3$ the maximum power levels for vorticity gusts are generally higher than those for entropy gusts, while for $\alpha_{eff} k^{1/2}/\beta_\infty > 0.3$ the opposite is generally true. At modest and high subsonic Mach numbers, the directivity patterns are a strong function of gust angle.

The results of this paper are relevant to a variety of applications. The isolated airfoil results presented here can be used directly for low solidity applications such as helicopter main rotors, with suitable modifications to account for finite span and blade rotation. For applications where cascade effects are important such as in aircraft engine blade/vane interactions, a high-frequency theory can be developed using a singular-perturbation structure similar to that employed in this paper. The influence of steady aerodynamic loading on the upstream radiation from a flat-plate cascade has been analysed in this manner by Peake & Kerschen (1997). The leading-edge ray field, which has been investigated parametrically in this paper, is a crucial element in their cascade prediction scheme.

The influence of airfoil thickness has not been considered in this paper, but can be analysed using similar methods. Additional sound source terms due to the thickness-related mean-flow perturbation appear in the local leading-edge region. In this local region, the contributions to the unsteady pressure field due to airfoil steady loading (camber and incidence angle) and airfoil thickness can be superposed. The global behaviour of the propagation of the sound field away from the leading-edge region and its subsequent scattering from the trailing edge can then be analysed along the same lines as in this paper, as will be made clear in a subsequent publication (Kerschen, Tsai & Reba 1998).

Much of the work described herein was funded by NASA Lewis Research Center under grant NAG3-357. We gratefully acknowledge this support. We thank Prof. T. F. Balsa and other colleagues at the University of Arizona for many stimulating and productive discussions. We also express our gratitude for computer support from the Division of Electronics and Computer Science of the FDA, in particular the assistance of Jonathon Boswell. Finally, we especially thank Ramons Reba for his thorough and insightful critiques of this work.

Appendix

This Appendix contains the directivity functions for the geometric acoustic field emanating from the airfoil leading edge.

D_0:

$$D_0(\theta) = -\frac{A_n \mathrm{e}^{-i\pi/4} \cos\tfrac{1}{2}\theta}{\beta_\infty(\pi(\delta + w))^{1/2}(\delta - w\cos\theta)};$$

D_1:

$$D_1(\theta) = \frac{\mathrm{i}2A_n\delta}{w^{1/2}(\delta - w\cos\theta)^{3/2}};$$

D_2:

$$D_2(\theta) = D_{2_p}(\theta) + D_{2_c}(\theta),$$

$$D_{2_p}(\theta) = \frac{-\mathrm{i}(\delta - w\cos\theta)f_1(-w\cos\theta) + k_n f_2(-w\cos\theta)}{4\,(\delta^2 + k_n^2)(2w\,(\delta - w\cos\theta))^{1/2}(\lambda_1 + w\cos\theta)\,(\lambda_2 + w\cos\theta)},$$

$$D_{2_c}(\theta) = -\left[4(\lambda_1 - \lambda_2)\,(\mathrm{i}k_n C_4 + \mathrm{i}\delta C_3) + \frac{(\lambda_1 + w)^{1/2} f_2(\lambda_1)}{(\lambda_1 + \delta)^{1/2}(\lambda_1 + w\cos\theta)} - \frac{(\lambda_2 + \delta)f_2(\lambda_2) + \mathrm{i}k_n f_1(\lambda_2)}{((\lambda_2 - w)\,(\lambda_2 + \delta'))^{1/2}(\lambda_2 + w\cos\theta)}\right]\frac{\cos\tfrac{1}{2}\theta}{4(\lambda_1 - \lambda_2)(\delta^2 + k_n^2)};$$

$$f_1(\lambda) = [\mathrm{i}C_2 - 2C_4(\lambda + \delta)]\,(-\delta^2 + k_n^2 - w^2 - 2\delta\lambda) + [C_1 + 2\mathrm{i}C_3(\lambda + \delta)]2\mathrm{i}k_n(\lambda + \delta),$$

$$f_2(\lambda) = [\mathrm{i}C_2 - 2C_4(\lambda + \delta)]\,2\mathrm{i}k_n\,(\lambda + \delta) + [C_1 + 2\mathrm{i}C_3(\lambda + \delta)](-\delta^2 + k_n^2 - w^2 - 2\delta\lambda),$$

$$\lambda_{1,2} = -\frac{\delta}{2}\left[\frac{\delta^2 + k_n^2 + w^2}{\delta^2 + k_n^2}\right] \pm \frac{\mathrm{i}k_n}{2}\left[\frac{\delta^2 + k_n^2 - w^2}{\delta^2 + k_n^2}\right];$$

$$C_1 = \mathrm{i}2^{3/2}\,(\delta A_t^*/\beta_\infty - k_n A_n), \quad C_3 = -2^{1/2}A_t^*\,M_\infty^2/\beta_\infty^3,$$

$$C_2 = \mathrm{i}2^{3/2}\,(k_n A_t^*/\beta_\infty + \delta A_n), \quad C_4 = -2^{1/2}A_n M_\infty^2/\beta_\infty^2;$$

D_3:

$$D_3(\theta) = \frac{\mathrm{i}A_n}{(w(\delta - w\cos\theta))^{1/2}}\left[1 - \frac{M_\infty^2}{\beta_\infty^2} - \frac{\delta}{\delta - w\cos\theta}\right] + \frac{\mathrm{i}A_n(\gamma + 1)M_\infty^4}{w^{3/2}(\delta + w)^{1/2}\beta_\infty^4}\left[\frac{\delta}{2}\cos\theta - \frac{w}{4}\cos 2\theta\right].$$

In the expression for $D_{2_c}(\theta)$, the square roots $(\lambda_i + \delta)^{1/2}$ and $(\lambda_i + w)^{1/2}$ are to be evaluated by introducing branch cuts joining $-\delta(= -\beta_\infty^{-2})$ and $-w$ to infinity through the lower half-plane. The square roots $(\lambda_i + \delta')^{1/2}$ and $(\lambda_i - w)^{1/2}$ are to be evaluated by introducing branch cuts joining $-\delta'(= -\beta_\infty^{-2})$ and w to infinity through the upper half-plane (see MK95 for full details).

REFERENCES

Cheng, H. K. & Rott, N. 1954 Generalizations of the inversion formula of thin airfoil theory. *J. Rat. Mech. Anal.* **3**, 357–382.

Ffowcs Williams, J. E. & Hall, L. H. 1970 Aerodynamic sound generation by turbulent flow in the vicinity of a scattering half-plane. *J. Fluid Mech.* **40**, 657–670.

Ffowcs Williams, J. E. & Hawkings, D. L. 1969*a* Sound generation by turbulence and surfaces in arbitrary motion. *Phil. Trans. R. Soc. Lond.* A. **264**, 321–342.

Ffowcs Williams, J. E. & Hawkings, D. L. 1969*b* Theory relating to the noise of rotating machinery. *J. Sound Vib.* **l0**, 10–21.

Goldstein, M. E. 1978 Unsteady vortical and entropic disturbances of potential flows round arbitrary obstacles. *J. Fluid Mech.* **89**, 433–468.

Goldstein, M. E., Rosenbaum, B. M. & Albers, L. U. 1974 Sound radiation from a high-speed axial-flow fan due to the inlet turbulence quadrupole interaction. *NASA TN* D-7667.

Kerschen, E. J. & Myers, M. R. 1987 Perfect gas effects in compressible rapid distortion theory. *AIAA J.* **25**, 504–507.

Kerschen, E. J., Tsai, C. T. & Reba, R. A. 1998 Influence of airfoil thickness on sound generation by interaction with high-frequency gusts. *J. Fluid Mech.* (to be submitted).

Mani, R. 1974. Isolated rotor noise due to inlet distortion or turbulence. *NASA CR* 2479.

Morfey, C. L. 1971. Acoustic energy in non-uniform flows. *J. Sound Vib.* **14**, 159–170.

Myers, M. R. & Kerschen, E. J. 1992 The acoustic field of a near surface source at intermediate distances: a simple result using matched asymptotic expansions. *J. Acoust. Soc. Am.* **92**, 1743–1753.

Myers, M. R. & Kerschen, E. J. 1995 Influence of incidence angle on sound generation by airfoils interacting with high-frequency gusts. *J. Fluid Mech.* **292**, 271–304 (referred to herein as MK95).

Peake, N. & Kerschen, E. J. 1997 Influence of mean loading on noise generation by the interaction of gusts with a flat-plate cascade: upstream radiation. *J. Fluid Mech.* **347**, 315–346.